

Electron energization and thermal to non-thermal energy partition during earth's magnetotail reconnection

Cite as: Phys. Plasmas **29**, 052904 (2022); <https://doi.org/10.1063/5.0085647>

Submitted: 18 January 2022 • Accepted: 16 April 2022 • Published Online: 10 May 2022

 M. Oka,  T. D. Phan,  M. Øieroset, et al.

COLLECTIONS

Paper published as part of the special topic on [Plasma Physics from the Magnetospheric Multiscale Mission](#)



[View Online](#)



[Export Citation](#)



[CrossMark](#)

ARTICLES YOU MAY BE INTERESTED IN

[The EDR inflow region of a reconnecting current sheet in the geomagnetic tail](#)
Physics of Plasmas **29**, 052903 (2022); <https://doi.org/10.1063/5.0083169>

[Strong reconnection electric fields in shock-driven turbulence](#)
Physics of Plasmas **29**, 042304 (2022); <https://doi.org/10.1063/5.0077529>

[Turbulence-driven magnetic reconnection and the magnetic correlation length: Observations from Magnetospheric Multiscale in Earth's magnetosheath](#)
Physics of Plasmas **29**, 012302 (2022); <https://doi.org/10.1063/5.0071106>

[Submit Today!](#)

Physics of Plasmas

[Special Topic: Plasma Physics
of the Sun in Honor of Eugene Parker](#)

Electron energization and thermal to non-thermal energy partition during earth's magnetotail reconnection

Cite as: Phys. Plasmas **29**, 052904 (2022); doi: [10.1063/5.0085647](https://doi.org/10.1063/5.0085647)

Submitted: 18 January 2022 · Accepted: 16 April 2022 ·

Published Online: 10 May 2022



View Online



Export Citation



CrossMark

M. Oka,^{1,a)} T. D. Phan,¹ M. Øieroset,¹ D. L. Turner,² J. F. Drake,³ X. Li,⁴ S. A. Fuselier,^{5,6} D. J. Gershman,⁷ B. L. Giles,⁷ R. E. Ergun,⁸ R. B. Torbert,⁹ H. Y. Wei,¹⁰ R. J. Strangeway,¹⁰ C. T. Russell,¹⁰ and J. L. Burch⁵

AFFILIATIONS

¹Space Sciences Laboratory, University of California, Berkeley, California 94720, USA

²Space Exploration Sector, The Johns Hopkins Applied Physics Laboratory, Laurel, Maryland 20723-6099, USA

³University of Maryland, College Park, Maryland 20742, USA

⁴Dartmouth College, Hanover, New Hampshire 03755, USA

⁵Southwest Research Institute, San Antonio, Texas 78238, USA

⁶Department of Physics and Astronomy, University of Texas at San Antonio, San Antonio, TX 78249, USA

⁷NASA Goddard Space Flight Center, Greenbelt, Maryland 20771, USA

⁸University of Colorado LASP, Boulder, Colorado 80303, USA

⁹University of New Hampshire, Durham, New Hampshire 03824, USA

¹⁰University of California, Los Angeles, Los Angeles, California 90095, USA

Note: This paper is a part of the Special Collection: Plasma Physics from the Magnetospheric Multiscale Mission.

^{a)}Author to whom correspondence should be addressed: moka@berkeley.edu

ABSTRACT

Electrons in earth's magnetotail are energized significantly both in the form of heating and in the form of acceleration to non-thermal energies. While magnetic reconnection is considered to play an important role in this energization, it still remains unclear how electrons are energized and how energy is partitioned between thermal and non-thermal components. Here, we show, based on *in situ* observations by NASA's magnetospheric multiscale mission combined with multi-component spectral fitting methods, that the average electron energy $\bar{\varepsilon}$ (or equivalently temperature) is substantially higher when the locally averaged electric field magnitude $|E|$ is also higher. While this result is consistent with the classification of "plasma-sheet" and "tail-lobe" reconnection during which reconnection is considered to occur on closed and open magnetic field lines, respectively, it further suggests that a stochastic Fermi acceleration in 3D, reconnection-driven turbulence is essential for the production and confinement of energetic electrons in the reconnection region. The puzzle is that the non-thermal power-law component can be quite small even when the electric field is large and the bulk population is significantly heated. The fraction of non-thermal electron energies varies from sample to sample between $\sim 20\%$ and $\sim 60\%$, regardless of the electric field magnitude. Interestingly, these values of non-thermal fractions are similar to those obtained for the above-the-looptop hard x-ray coronal sources for solar flares.

© 2022 Author(s). All article content, except where otherwise noted, is licensed under a Creative Commons Attribution (CC BY) license (<http://creativecommons.org/licenses/by/4.0/>). <https://doi.org/10.1063/5.0085647>

I. INTRODUCTION

Magnetic reconnection converts magnetic energy to particle energy and can lead to explosive energy-release in magnetospheric, solar, and astrophysical plasma environments (e.g., Zweibel and Yamada, 2009; Ji and Daughton, 2011, and references therein). In this

process, electrons are heated to produce a hot thermal component. They can also be accelerated to very high, non-thermal energies. Despite decades of study, however, it remains unclear how electrons are energized and how energy is partitioned between thermal and non-thermal components. For solar flares, it has been reported that

non-thermal electrons alone carry up to 50% of the released magnetic energy (e.g., Lin and Hudson, 1976; Aschwanden *et al.*, 2017). This is in contrast to the case of earth's magnetotail where non-thermal electrons appear to carry only a minuscule fraction of released energy (e.g., Øieroset *et al.*, 2002; Eastwood *et al.*, 2013).

In earlier years of magnetotail exploration, electron energy spectra were studied in great detail by Christon *et al.* (1988; 1989; 1991) using data from the ISEE spacecraft. It was reported that the electron populations respond collectively as a single unified population (rather than separated thermal and non-thermal populations) during magnetotail activities and that the energy spectrum can be generally described by the kappa distributions, although there are often deviations from the kappa distribution, especially in the lower energy range. It was further reported that the power-law index δ (as measured in differential flux) can be ~ 4 or larger (Christon *et al.*, 1991), and that the power-law spectrum often remains hard even in undisturbed conditions as measured by the Auroral Electrojet (AE) index (Christon *et al.*, 1989).

In more recent decades, electron acceleration has been diagnosed more frequently in the context of magnetotail reconnection. It was reported that electrons are accelerated up to ~ 300 keV in the Hall region and that the power-law part of the spectrum (above a certain energy threshold) carries $\sim 10\%$ of the total electron energy (Øieroset *et al.*, 2002). There have also been numerous observations of electron acceleration associated with reconnection-related features such as the dipolarization front (or dipolarizing flux tubes) (e.g., Fu *et al.*, 2011; Birn *et al.*, 2014; Turner *et al.*, 2016; and Gabrielse *et al.*, 2017), flux ropes (e.g., Chen *et al.*, 2008; Retinò *et al.*, 2008) and their coalescence (e.g., Wang *et al.*, 2016), separatrix (e.g., Jaynes *et al.*, 2016; Norgren *et al.*, 2020), reconnection jets (or convective flows) (e.g., Asano *et al.*, 2010; Eriksson *et al.*, 2020; and Chen *et al.*, 2019a), electron-scale diffusion region (or the dissipation region) (e.g., Oka *et al.*, 2016; Cohen *et al.*, 2021; and Turner *et al.*, 2021), and turbulence (e.g., Ergun *et al.*, 2020b). These observations demonstrate a clear association between electron acceleration and many reconnection related, kinetic-scale phenomena. They often focus on a specific location or specific structure although a variety of different kinetic structures can exist in the same event. Also, there can be different stages in the magnetotail evolution. Thus, there is a need for an updated, large-scale picture of the electron energy spectra with different stages of magnetotail evolution considered. Such analysis would enable us to compare magnetotail observations with solar flare observations, which do not have information as detailed as *in situ* observations in space. Observations by NASA's Magnetospheric Multiscale (MMS) mission (Burch *et al.*, 2016) are ideal for such a study. MMS provides measurements of full 3D velocity distributions of ions and electrons as well as all three components of the electric and magnetic fields. The particle measurements by two different instruments cover a wide energy range from 10 eV to 500 keV, and all data have been well calibrated.

Thus, the main purpose of this paper is to update our overall, large-scale picture of electron energy spectra in the magnetotail in the context of reconnection by using the comprehensive data set obtained by MMS. Rather than focusing on the small-scale kinetic structures associated with magnetic reconnection, we will examine large-scale evolution of electron energy spectra across the reconnection region (more specifically, the Hall region). Particularly new in our study is the consideration of different preconditioning (or magnetotail activity level).

Previous studies of the global evolution of the magnetotail led to the picture of two-step energy release (e.g., Hones, 1977; Baker *et al.*, 2002; and Cao *et al.*, 2008). It was argued that the magnetic X-line progresses from reconnection of closed (plasma sheet) to open (lobe) field lines. The open (lobe) field reconnection (with the concomitant large Alfvén speeds in the inflow region) is more explosive and marks the pinching off of the plasmoid (Baker *et al.*, 2002). The pictures of plasma-sheet and tail-lobe reconnection, including how they are related to the open/closed configurations, are well illustrated in, for example, Fig. 3 of Hones (1977) and Fig. 5 of Baker *et al.* (2002).

It remains unclear precisely how reconnection becomes explosive and how particles gain energies during reconnection, but it is instructive to consider a possible importance of the reconnection electric field E_R . The reconnection electric field E_R can be expressed as $E_R = \alpha_R V_A B_0$, where α_R is the reconnection rate (typically estimated as ~ 0.1), B_0 is the magnetic field magnitude in the inflow region, N is the number density of the current sheet, and V_A is the Alfvén speed obtained from B_0 and N defined above. Then, if particles were able to feel this electric field (in the current sheet where particles are unmagnetized), the particle energy gain $\Delta\varepsilon$ would be expressed as $\Delta\varepsilon = qE_R L$, where q is particle charge and L is the size of the energy-release site. When normalized, it becomes

$$\Delta\varepsilon = \alpha_R \left(\frac{L}{d_i} \right) m_i V_A^2, \quad (1)$$

where d_i is the ion inertia length. Thus, if the reconnection rate and the size of the reconnection region were the same, the tail-lobe reconnection which has a larger value of B_0 and a smaller value of N results in an enhanced energization of particles by the enhanced V_A and E_R . This is of course a naive discussion, and the precise mechanism of particle energization is not fully understood yet. Nevertheless, Eq. (1) provides a possible explanation of the importance of the Alfvén speed as suggested by, for example, Baker *et al.* (2002).

More intuitively, the dependence on the Alfvén speed V_A^2 is described as how much magnetic energy is available per particle or how strongly particles are magnetized because $m_i V_A^2 / 2 = B^2 / 8\pi N$ (e.g., Kennel and Petschek, 1966). In the presence of inflows and hence Poynting flux, the total electromagnetic energy per particle available for reconnection can be expressed as $m_i V_A^2$ by dividing the incoming Poynting flux by the inflowing particle density flux (e.g., Shay *et al.*, 2014).

This paper is organized as follows: We first review the kappa and flattop distributions, which serve as the basis of our spectral analysis (Sec. II). We then describe the instrumentation and data set used in this study (Sec. III). In the main section (Sec. IV), we present three cases of magnetotail reconnection (events A, B, and C) to demonstrate the variation of the spectral forms. Events A and C (earlier phase) are the plasma-sheet reconnection whereas events B and C (later phase) are the tail-lobe reconnection. Also we use all three cases to compare the average electron energy with the average electric field magnitude. Finally, we summarize the observations and discuss the results (Sec. V).

II. SPECTRAL MODELS

In this paper, we analyze omni-directional electron data, i.e., the energy spectra averaged over all directions, at a reduced time resolution. While electrons often exhibit anisotropy or beam features at the fine scales, fitting those features requires the analyses to be performed in 2D or 3D velocity space, which is well beyond the scope of this

paper. Our idea here is to start from a simple approach of assuming isotropy and obtain a rough, overall picture of how electrons are energized and partitioned between thermal and non-thermal components. Our approach may not be applicable to the kinetic scale or shorter timescale variations where electrons exhibit more complicated velocity distribution functions. It is also to be emphasized that, in our definition, a plasma population is “non-thermal” if it exhibits a power-law in the energy spectrum. Thus, an isolated beam component would still be included in the thermal component if the speed of the beam was small and if it did not exhibit a power-law. We confirmed, however, that such cases are rare and do not affect the main conclusion of this paper.

With all these assumptions, we examine 1D energy spectra at a reduced time resolution (more details of the data analysis will be presented later). In our spectral analysis, we use Maxwellian (f_M), kappa (f_κ), flattop (f_{FT}) distributions, and a combination of these distributions. This choice has been developed through an iterative process of visually inspecting all samples and confirming that the data can be reasonably fitted with at least one of these models. Below, we describe more details of the key models.

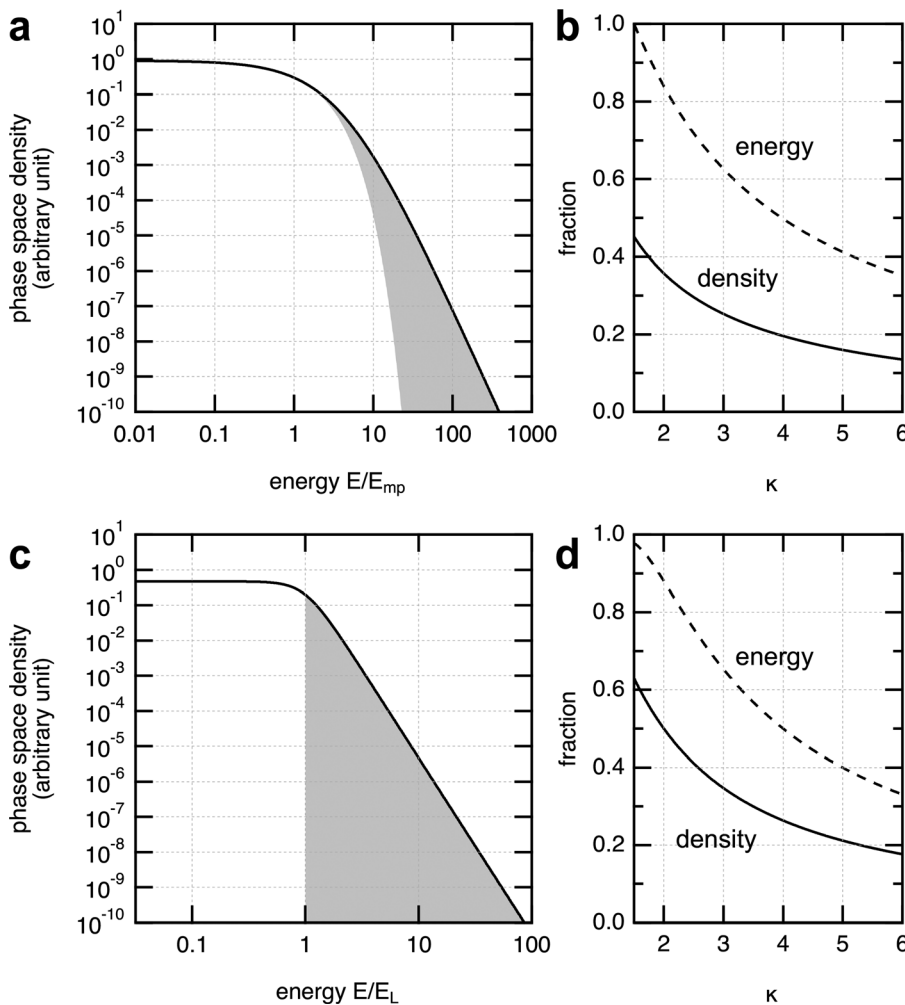


Figure 1 illustrates the kappa and flattop distributions. Assuming isotropic distribution with zero bulk flow speed, the phase space density $f(v)$ of the kappa distribution is expressed as

$$f(v) = A \left[1 + \left(\frac{v^2}{\kappa \theta^2} \right) \right]^{-(\kappa+1)}, \quad (2)$$

where

$$A \equiv \frac{N}{(\pi \kappa \theta^2)^{3/2}} \frac{\Gamma(\kappa+1)}{\Gamma(\kappa-1/2)}, \quad (3)$$

v is the particle speed, N is the density, θ is the most probable speed at which the differential flux becomes maximum, and κ is the power-law index (e.g., Olbert, 1968). κ is defined so that it matches with the power-law index δ as measured in differential flux. The kappa distribution is a fundamental form that can be obtained by maximizing the entropy in the Tsallis statistics, which is an extension of the Boltzmann–Gibbs statistics to include a power-law distribution (e.g., Milovanov and Zelenyi, 2000; Leubner, 2002). In fact, the kappa

FIG. 1. Key spectral models used in this study: [(a) and (b)] kappa and [(c) and (d)] flattop distributions. For each model, the spectral form is shown for the $\kappa=4$ case with the energy normalized by $E_{mp} (\equiv kT_M)$ and $E_L (\equiv 1/2mv_L^2)$ for the (a) kappa and (c) flattop distributions, respectively. The gray shaded region indicates our definition of the non-thermal component. The non-thermal fractions of densities (solid curve) and energies (dashed curve) are also shown as a function of κ [panels (b) and (d)]. See texts for more details.

distribution approaches to a power-law at its higher-energy end and approaches a Maxwellian distribution at its lower-energy end. While a Maxwellian distribution represents the thermal equilibrium, the kappa distribution can be reproduced by considering thermalization in the presence of turbulence that provides stochasticity needed for a power-law formation (e.g., Ma and Summers, 1998; Yoon *et al.*, 2006; and Bian *et al.*, 2014). The average energy of particles E_{avg} can be expressed as

$$\begin{aligned} E_{\text{avg}} &= \frac{3}{2} k_B T_\kappa \\ &= \frac{3}{2} k_B T_M \left(\frac{\kappa}{\kappa - 3/2} \right), \end{aligned} \quad (4)$$

where T_κ is the kappa temperature and T_M is defined as $k_B T_M \equiv 1/2m\theta^2$.

For convenience, we follow recent solar flare studies (Oka *et al.*, 2013; 2015) and define a thermal core component with the temperature $k_B T_M$. The difference between the kappa and core distributions (the shaded region in Fig. 1) represents the non-thermal component. One may introduce another definition of non-thermal fraction by using a sharp cutoff at energy E_c to separate thermal and non-thermal components. However, such a definition requires an arbitrary choice of E_c . In our definition, the core temperature $k_B T_M$ serves the role of E_c but is determined naturally from the kappa distribution form. As a result, the non-thermal fractions of particle density and energy can be calculated analytically. Here, the non-thermal fraction of particle density R_N is defined as $R_N = N_{\text{nt}}/N_{\text{tot}}$, where N_{nt} is the density of the non-thermal component and N_{tot} is the total density derived from the entire energy spectrum. Similarly, the non-thermal fraction of particle energy R_e is defined as $R_e = \varepsilon_{\text{nt}}/\varepsilon_{\text{tot}}$, where ε_{nt} is the energy density of the non-thermal component and ε_{tot} is the energy density derived from the entire energy spectrum. The calculated values of R_N and R_e are illustrated in Fig. 1(b) as a function of κ . It indicates that $\kappa \sim 4$ marks the equipartition between thermal and non-thermal energies.

The flattop distribution has been observed at earth's bow shock (Feldman *et al.*, 1982), interplanetary shocks (Feldman *et al.*, 1983), and in earth's magnetotail (e.g., Asano *et al.*, 2008; Chen *et al.*, 2009; Wang *et al.*, 2010; Egedal *et al.*, 2010; Oka *et al.*, 2016; and Teh *et al.*, 2018). It has been argued that, at collisionless shocks, the flattop distribution is associated with electron heating that results in part from energization by a cross-shock potential, followed by beam driven instabilities (Feldman *et al.*, 1983; Thomsen *et al.*, 1983). For the magnetotail, the flattop distribution has been associated with the reconnection separatrix (Asano *et al.*, 2008), magnetic islands (or flux rope in 3D) (Chen *et al.*, 2009; Wang *et al.*, 2010; and Teh *et al.*, 2018), the reconnection inflow region (Egedal *et al.*, 2008), and immediate downstream of the electron-scale diffusion region (Oka *et al.*, 2016). Interestingly, the model by Egedal *et al.* (2008) involves a potential that works on an electron as it escapes the region along a magnetic field line. Thus, there is a similarity in the formation of the flattop distribution in the shock and reconnection regions.

The phase space density $f(v)$ of the flattop distribution is expressed as

$$f(v) = A \left[1 + \left(\frac{v}{v_L} \right)^{2\kappa} \right]^{-\frac{\kappa+1}{\kappa}}, \quad (5)$$

where

$$A \equiv \frac{3N}{2\pi v_L^3} \frac{\Gamma(1/\kappa)}{\Gamma(1+3/2\kappa)|\Gamma(-1/2\kappa)|}, \quad (6)$$

v_L is the “shoulder speed” below which the phase space density becomes constant (and the spectral form becomes flat), and the other parameters are the same as those of the kappa distribution. This expression is an isotropic version of the flattop distribution given by Thomsen *et al.* (1983). The spectrum becomes a power-law above v_L (or the shoulder energy of $E_L \equiv 1/2mv_L^2$). The average energy of particles E_{avg} can be expressed as

$$\begin{aligned} E_{\text{avg}} &= \frac{3}{2} k_B T_{FT} \\ &= \frac{3}{2} E_L \left[\frac{2 \Gamma(1+5/2\kappa)\Gamma(-3/2\kappa)}{5 \Gamma(1+3/2\kappa)\Gamma(-1/2\kappa)} \right], \end{aligned} \quad (7)$$

where T_{FT} is the temperature of the flattop distribution.

In principle, we cannot define a non-thermal fraction for the flattop distribution because any part of the distribution cannot be approximated by a thermal Maxwellian distribution. In fact, unlike the kappa distribution, the flattop distribution does not approach to the Maxwellian distribution in the $\kappa \rightarrow \infty$ limit. It approaches to a step function, i.e., $f(E) = A$ in the $E < E_L$ range and $f(E) = 0$ in the $E > E_L$ range. Thus, in this study, we tentatively regard the spectral part in the $E < E_L$ and $E > E_L$ ranges as the thermal and non-thermal component, respectively. With this definition, the non-thermal fractions, R_N and R_e , can be evaluated analytically. The result is shown in Fig. 1(d). The dependence on κ is slightly different from that of the kappa distribution, but $\kappa \sim 4$ again marks the equipartition of energy.

When fitting the data, we considered a total of 8 spectral models as listed below:

- f_M ,
- $f_{M,\text{cold}} + f_\kappa$,
- $f_{M,\text{cold}} + f_\kappa + f_{M,\text{hot}}$,
- $f_{M,\text{cold}} + f_{FT} + f_{M,\text{hot}}$,
- f_κ ,
- $f_\kappa + f_{M,\text{hot}}$,
- f_{FT} , and
- $f_{FT} + f_{M,\text{hot}}$.

Here, $f_{M,\text{cold}}$ and $f_{M,\text{hot}}$ represent the same Maxwellian distribution but with low and high temperature values, respectively. They are controlled by the initial values in each fitting. Also, the components are shown in order of temperature (or average energy of particles). For example, in the $f_{M,\text{cold}} + f_\kappa + f_{M,\text{hot}}$ model, the temperature of the kappa distribution is smaller than that of $f_{M,\text{hot}}$. Upon calculating the non-thermal fraction, $f_{M,\text{hot}}$ is regarded as a non-thermal component because its temperature is higher than that of the main plasma population (represented by f_κ or f_{FT}). The density of this component is usually very small, so it does not greatly affect the non-thermal fraction. It is also to be noted that this component represents an enhancement (or a “bump”) at the higher energy range and, thus, different from the exponential cutoff of the power-law tail, which is generally represented by $E^{-\gamma} \exp(-E/E_{\text{cutoff}})$. We did not find such a smooth, exponential cutoff of the power-law tail in the events presented in this paper.

III. INSTRUMENTATION AND DATA SET

We use publicly available, level-2 data from NASA's MMS mission (Burch *et al.*, 2016). We use magnetic and electric field data obtained by the FIELDS instrument (Russell *et al.*, 2016; Lindqvist *et al.*, 2016; and Ergun *et al.*, 2016) as well as particle data obtained by the *Fast Plasma Investigation* (FPI) (Pollock *et al.*, 2016), the Energetic Particle Detector (EPD) (Blake *et al.*, 2016), and the *Hot Plasma Composition Analyzer* (HPCA) (Young *et al.*, 2016). The electron data come from FPI and EPD [primarily *Fly's Eye Energetic Particle Sensor* (FEEPS)] to cover both lower and higher energy ranges, respectively. For ion moments (velocity vectors and temperatures), we use data from HPCA because HPCA has a larger energy coverage and enables a consistent calculation of moments even during periods of intense energization associated with reconnection. All data are shown in Geocentric Solar Magnetospheric (GSM) coordinates.

Because we focus on average properties of electron energy spectra, we will use the survey-mode data that are continuously available throughout the events of interest. Unless otherwise noted, the energy spectra presented in this paper are obtained for a ~ 9 s period, which typically contains two samples of Fast Plasma Investigation (FPI) fast-survey-mode data and four samples of FEEPS survey-mode data. The time resolution of the HPCA data (ion moments) is ten seconds and, thus, sufficient to be compared with the survey-mode electron data. We examined some of the higher-resolution burst-mode data whenever available and confirmed that our conclusion of this paper is not sensitive to the choice of the data mode. Also, while there are four identical spacecraft in the MMS mission, we primarily use data from MMS-3. Because of the short inter-spacecraft distance, all four spacecraft observe basically the same features at similar timing, and thus our results and conclusions are not sensitive to the choice of spacecraft.

Upon analysis of electron energy spectra, we removed data points that are contaminated by photoelectrons. We also removed noisy data that are close to the detection limit (i.e., the one-count-level falls within the error range of the signal). Then, we fitted the data with the spectral models described in Sec. II. More details of the data point removal as well as the technical procedure of spectral fitting are described in Appendices A and B, respectively.

IV. OBSERVATIONS

We now present specific examples of electron energy spectra obtained in three different events featuring magnetotail reconnection. Events A and B provides good examples of plasma-sheet and tail-lobe reconnection, respectively. Event C illustrates the transition between the two phases. In all three events, the MMS spacecraft stayed very close to the plasma sheet center for a relatively long time, enabling us to investigate the average picture of electron energy spectrum in the plasma sheet. We also confirmed, by following the technique described by Eastwood *et al.* (2010), that all these exhibit the quadrupole structure of the out-of-plane magnetic and/or the bipolar structure of the in-plane electric field. Thus, all these events can be described as the Hall reconnection.

A. Event A: Plasma-sheet reconnection

Figure 2 shows an overview of event A observed by MMS3. Observations are shown for 22:00–23:00 UT of July 11, 2017 and the

time period of reconnection signature (especially high speed flows) is highlighted in yellow. The sign of the sunward-earthward component of the high-speed plasma flow (V_{ix}) reversed from negative to positive at around 22:34–22:37 UT [the blue curve in Fig. 2(e)], indicating that the reconnection X-line passed by MMS and convected in the tailward direction. A close inspection revealed that there was a correlated reversal of the north-south component of the magnetic field (B_z) as well as the electron-scale diffusion region (EDR) at around 22:34 UT. More details can be found in earlier reports of this event (e.g., Torbert *et al.*, 2018; Genestreti *et al.*, 2018; Nakamura *et al.*, 2018; 2019; and Burch *et al.*, 2019).

Here, we focus on the variation of the energetic electron flux at larger time-scales, as shown in Figs. 2(d) and 2(j). The energetic electron flux increased roughly with a decreasing distance from the X-line, as can be seen in the green-color region of the spectrogram in Fig. 2(d). However, the flux was consistently high on the earthward side of the X-line (i.e., after the X-line passage), as can be seen in the 80 keV flux profile in Fig. 2(j). Across the reconnection encounter, the temperature remained relatively constant at ~ 5 keV [Fig. 2(f)] but there were significant fluctuations in the magnetic and electric fields [Figs. 2(b) and 2(h)]. The density remained high at or above $\sim 0.1 \text{ cm}^{-3}$ throughout the event, and the AE index (measured by the THEMIS network of ground stations) remained low.

Figure 3 shows three examples of the electron energy spectra obtained in event A, demonstrating the typical features especially the kappa-like spectral form. It is evident that the non-thermal tail was less enhanced before reconnection (spectrum 1), but it is enhanced substantially in the reconnection region and exhibited a power-law form (spectrum 2). Then, the power-law spectrum became soft again after reconnection (spectrum 3). This variation is seen clearly seen in Fig. 2(k), which shows the time variation of κ through the event (pink curve). κ starts to decrease around 22:00 UT and reaches a minimum around 22:35 UT, near the flow reversal (and the presumed X-line location), and increases again following the X-line encounter. Such a variation is consistent with an earlier report that showed a spectral hardening toward the center of the ion-scale diffusion region (or the Hall region) (e.g., Øieroset *et al.*, 2002). It is also clear that, in all three spectra shown in Fig. 3, the entire energy spectrum is generally represented by the kappa distribution model, as shown in the left column [i.e., Figs. 3(a), 3(d), and 3(g); purple curves]. As a general rule of thumb, the reduced chi-square (χ^2_ν) should be of the order of ~ 1 for a successful fit. In this sense, the kappa distribution model fits the data reasonably well because χ^2_ν was in the range from 1 to 4. It is to be emphasized that, in all three spectra, there is no clear “spectral break” that separates the thermal and non-thermal components, suggesting that the energy spectrum is dominated by a single unified population. This is consistent with the reports from the ISEE era (Christon *et al.*, 1988; 1989; 1991). Using the kappa distribution model, the non-thermal fraction of electron energy R_e is estimated. It varied from 19% to 52% and then 31%, as annotated in Figs. 3(a), 3(d), and 3(g), and also seen in Fig. 2(e), which shows the variation of R_e through the entire event.

Interestingly, a close inspection reveals that the data are not always described perfectly by the kappa distribution and that the non-thermal fraction can be sensitive to the choice of the model. For spectrum 1, there was a substantial deviation from the kappa distribution model in the lower energy (<0.3 keV) range [Fig. 3(a)]. The deviation

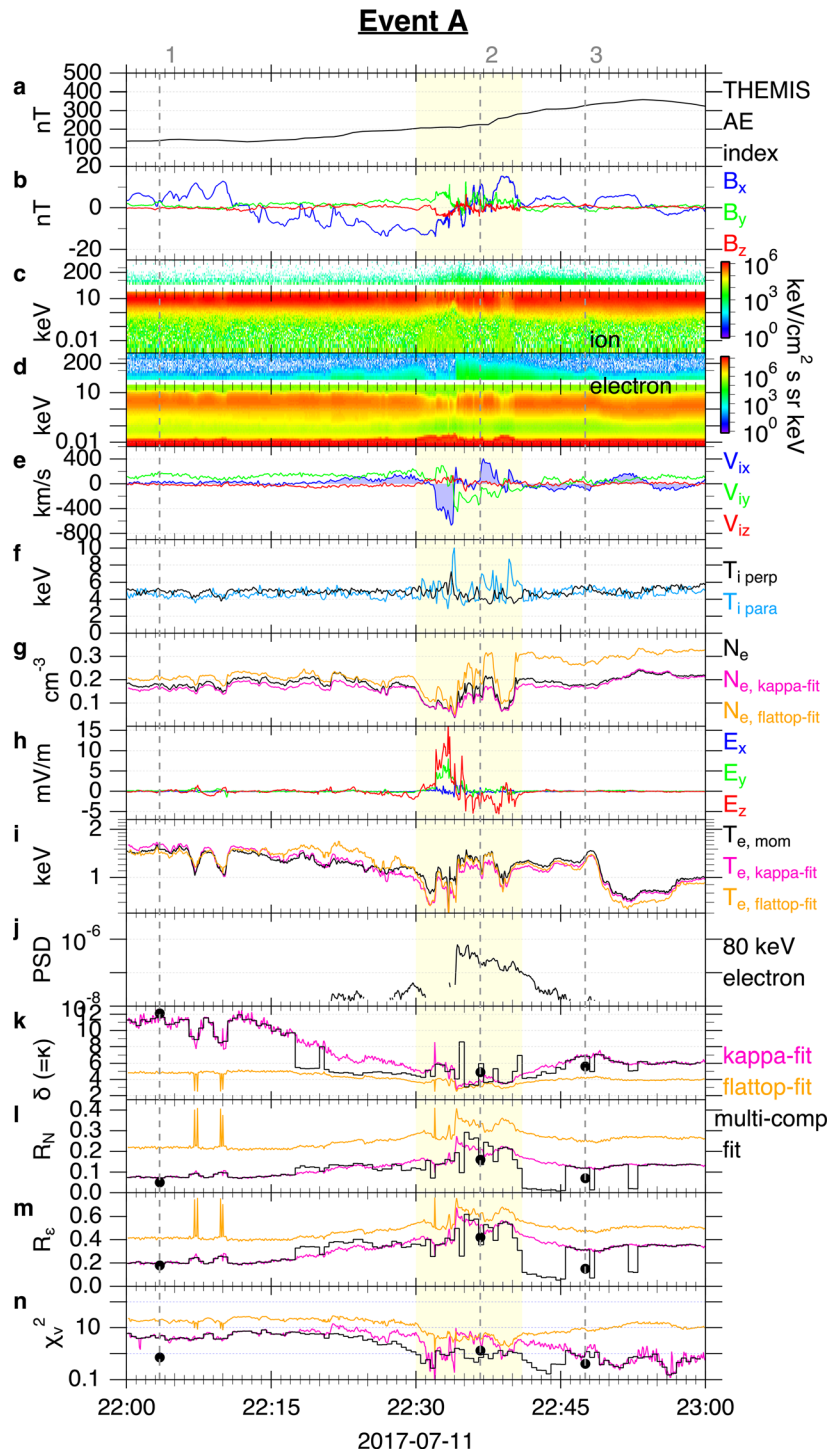


FIG. 2. Overview of event A (July 11, 2017). The reconnection region is highlighted in yellow. From top to bottom are (a) THEMIS AE index, (b) magnetic field, (c) and (d) ion and electron energy spectrograms, (e) ion bulk flow, (f) perpendicular and parallel ion temperatures, (g) electron density, (h) electric field, (i) electron temperature, (j) phase space density (s^3/km^6) of ~ 80 keV electrons, (k) power-law index δ , (l) and (m) non-thermal fraction of electron densities R_N and energies R_e , respectively, and (n) reduced chi-square χ^2 . The pink and orange curves are obtained by fitting energy spectra with the kappa and flattop models, respectively. The black stepped lines are obtained by fitting 5 min data with multi-component models. The vertical dashed lines indicate the times of energy spectra shown in Fig. 3. The filled black circles indicate the best-fit parameters as shown in Fig. 3.

is modeled by an additional Maxwellian distribution, as shown in the multi-component model [Fig. 3(c), thick gray curve]. The energy range is still above the spacecraft potential (15 V). Thus, this additional component can be interpreted as a cold plasma population in the plasma

sheet. Adding such a cold population does not substantially change the non-thermal fractions in this specific case. Similar cold populations have been reported previously (e.g., Christon *et al.*, 1991), but its origin remains unclear (Delzanno *et al.*, 2021). For spectrum 2, the kappa

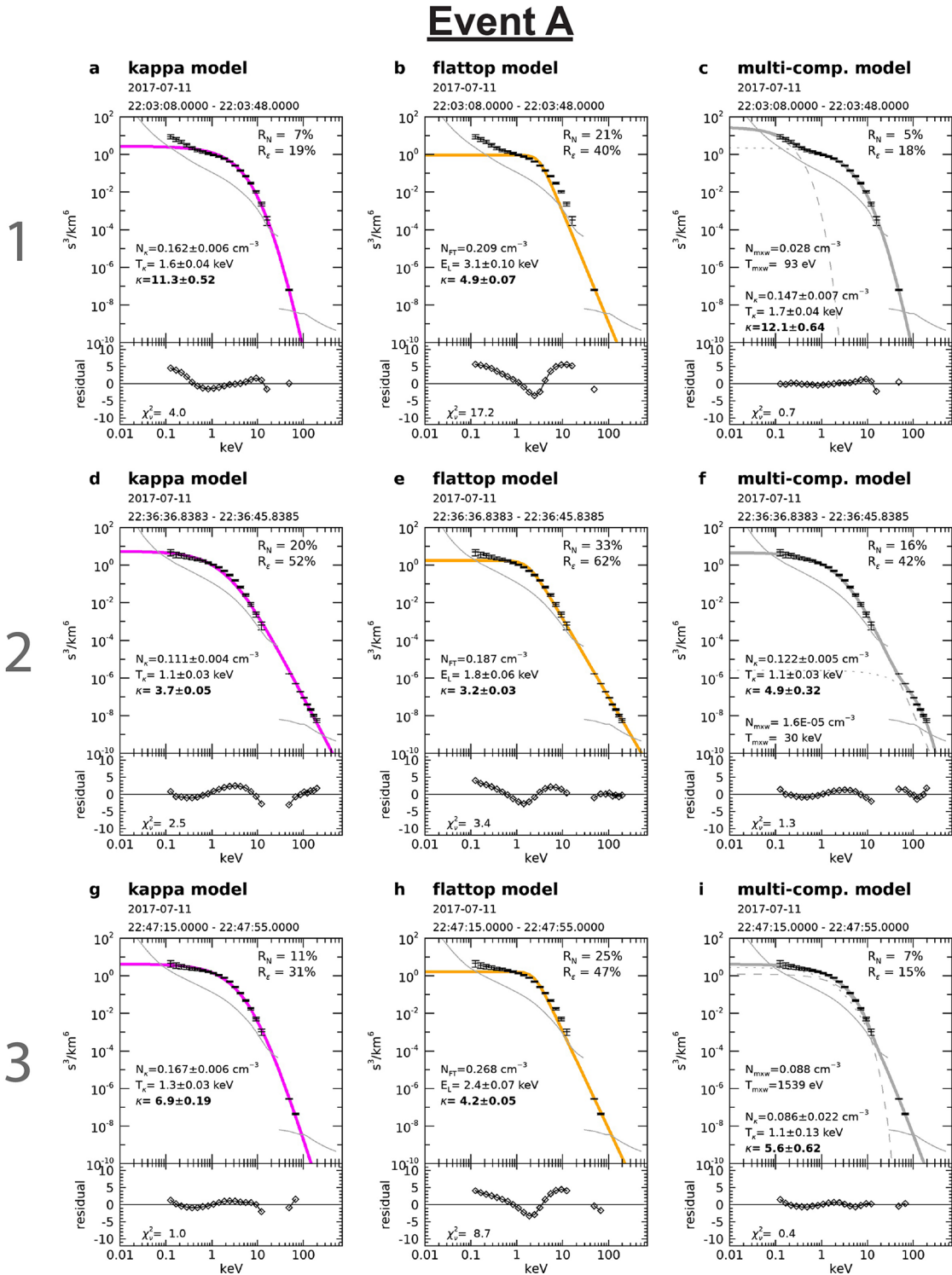


FIG. 3. Example analyses of electron energy spectra obtained in event A (July 11, 2017). Three different spectra are shown (top, middle, and bottom rows) with three different model fitting (left, center, and right columns). The spectra are obtained at the times marked by the vertical dashed lines in Fig. 2. The black marks with error bars are the values measured by the FPI ($< 30 \text{ keV}$) and FEEPS ($> 30 \text{ keV}$) instruments. The thin gray curves indicate the detection limit (i.e., one-count-level). The best-fit models are shown in color, i.e., the kappa distribution (purple curves), flattop distribution (orange curves), and the multi-component model (gray curves). The best-fit parameters are annotated in each panel. The residuals are normalized, as described in Appendix B.

distribution model again fits the data well. However, a slight deviation remains and the other spectral models, i.e., flattop and the combined (Maxwellian + kappa distribution) models, can also fit the data equally well in a sense that their χ^2_ν is of the order of unity [Figs. 3(e) and 3(f)]. This leads to a large ambiguity in our estimate of the non-thermal fraction. This fraction is as small as 42% in the multi-component model and as large as 62% in the flattop model. Thus, spectrum 2 illustrates an example of those cases where it is difficult to automatically and programmatically interpret the data without any assumption. For spectrum 3, the flattop distribution model does not fit the data well, as indicated by the relatively large χ^2_ν . On the other hand, the multi-component model fits the data too well, leading to a substantially small $\chi^2_\nu (< 1)$. This is often described as an “over-fitting” (e.g., Andrae *et al.*, 2010). In principle, any spectral form can be fitted better by adding an extra spectral component or using a spectral model with a larger number of free fitting parameters. In this study, we favor a spectral model that produces χ^2_ν of order of unity with the smallest number of parameters, see also Appendix B.

The time variation of the quantities derived from the fitting are shown in Figs. 2(k)–2(n). The single functional models such as the kappa (pink curves) and flattop (orange curves) models show smooth profiles although χ^2_ν is mostly large. The multi-component model leads to a large fluctuations of non-thermal fractions, as described above, so we performed spectral fitting after reducing the time resolution down to 30 s (thin stepped lines). During the time period when χ^2_ν is reasonable (~ 1), the non-thermal fraction of energies, R_e , varied between 20% and 60%.

B. Event B: Tail-lobe reconnection

Figure 4 shows an overview of event B with the time series of various plasma parameters obtained by MMS3. The data are shown for 07:10–07:53 UT of July 26, 2017 and the time period of reconnection signature (especially high-speed flows) is highlighted in cyan. Similar to event A, a correlated V_{ix} and B_z reversal is identified (both from negative to positive) [Fig. 4(e)], indicating that a reconnection X-line passed by the spacecraft in the tailward direction. However, unlike event A, there was an intensification of both magnetic [Fig. 4(b)] and electric [Fig. 4(h)] field turbulence. More details of the key reconnection features and associated turbulence of this event can be found in Ergun *et al.* (2020b; 2020a).

Here, we emphasize that flow speeds were much higher when compared to event A and that they reached ~ 2000 km/s [Fig. 4(e)]. The electron temperature was also enhanced by an order of magnitude [Fig. 4(i)], although it was almost constant across the reconnection region in event A. Also, the incident plasma density depleted substantially [Fig. 4(g)].

These features of enhanced temperature and depleted density are consistent with the picture of plasma-sheet reconnection in which the preexisting, dense plasmas were pushed away by reconnection and the tenuous lobe plasma starts to flow in. It has been argued that the incoming open field lines (with the concomitant large Alfvén speeds) lead to a more explosive behavior including enhanced temperature (e.g., Baker *et al.*, 2002).

Figure 5 shows three examples of electron energy spectra obtained in event B, demonstrating three features that were not seen in event A. The most striking feature is that the non-thermal flux was high and the spectrum was hard even before the encounter with the

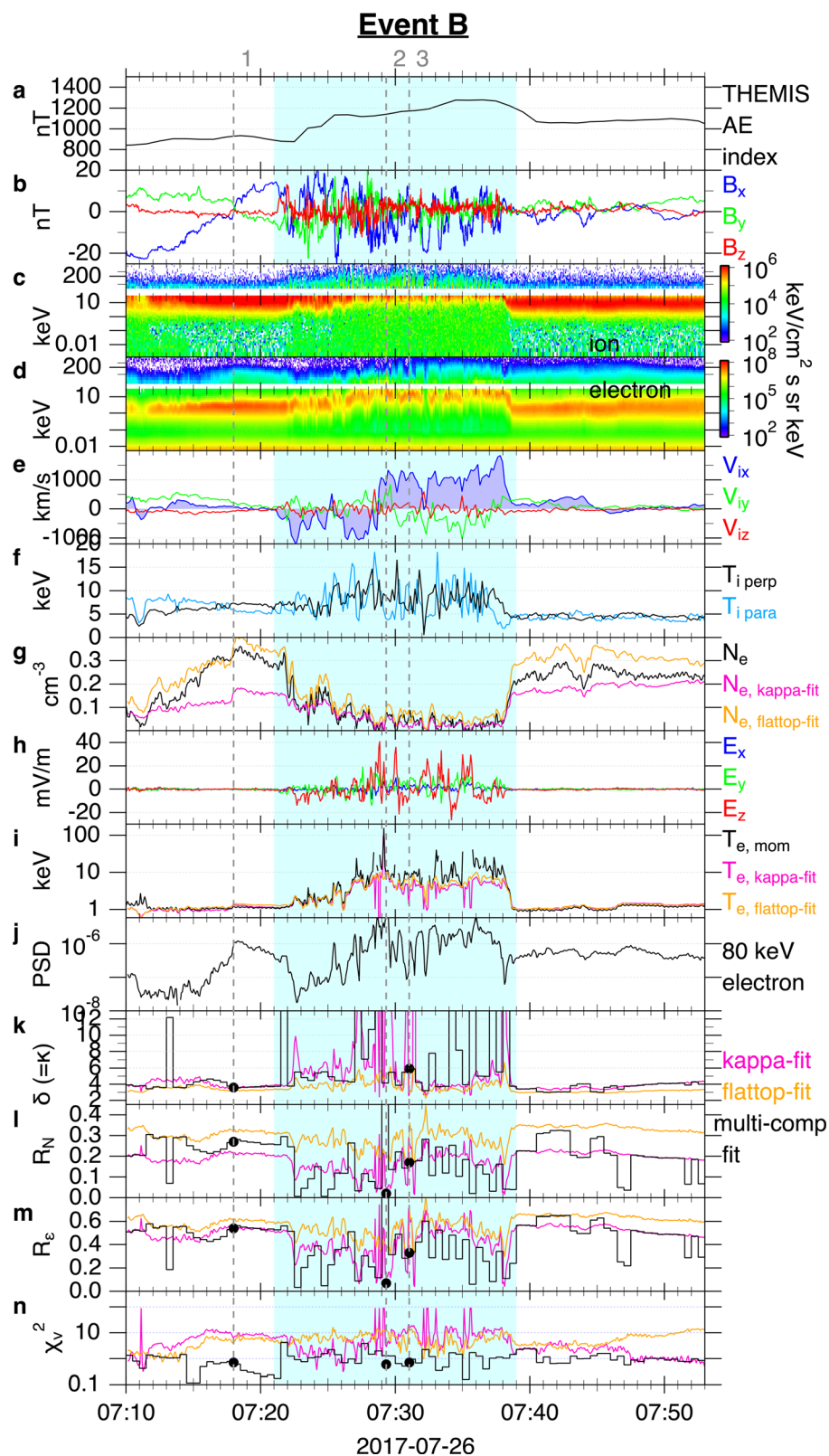
reconnection region, as shown in spectrum 1. For this specific case of spectrum 1, the kappa distribution alone did not fit the data well. A three-component model, $f_{M,\text{cold}} + f_{FT} + f_{M,\text{hot}}$, was necessary to obtain a reasonably good fit, i.e., $\chi^2_\nu \sim 1$. Similar cases of enhanced energetic electron flux were seen both before and after the encounter [Fig. 4(j)]. The kappa distribution model alone did not fit the data reasonably well ($\chi^2_\nu > 1$) during 07:15–07:21 UT and 07:39–07:47 UT. The kappa distribution model fitted the data reasonably well further outside the reconnection region (before 07:11 UT and after 07:48 UT), but the power-law spectrum remained equally hard ($\delta \sim 4$). These observations indicate that energetic, non-thermal electrons were prevalent outside the reconnection region.

Another key feature of event B is that the non-thermal power-law tail was not always obvious during reconnection, as shown in spectrum 2. This spectrum was obtained when the electron temperature was the highest (Fig. 4, the second vertical dashed line). Both the kappa distribution [Fig. 5(d)] and multi-component [Fig. 5(f)] models fit the data reasonably well. The results indicate that the temperature of the main population was ~ 10 keV. The power-law index κ was very large, suggesting that the main component was very close to a Maxwellian. The computed non-thermal fraction of electron energy R_e was $\lesssim 10\%$. Such a small R_e is also illustrated in Figs. 4(l) and 4(m).

Event B was also different from event A in a sense that it often exhibited a clear flattop feature, as shown in spectrum 3 [Figs. 5(g)–5(i)]. However, there was also an additional high-energy component above ~ 80 keV, and the flattop distribution alone did not fit the data well. It is to be noted again that the shoulder energy ($E_L \sim 17$ keV in this case) is different from the effective temperature ($T_{FT} \sim 2.6$ keV) because of Eq. (7). Also, the high-energy component was fitted by the Maxwellian distribution with unrealistically high temperature (~ 73 keV) just to avoid over-fitting. One may interpret this component as a single power-law or a power-law with a roll-off at its high-energy end (around 200 keV in this case). However, such models require an additional free parameter to fit the data and would lead to over-fitting. As described in Sec. IV A, we looked for the model that can reasonably fit the data well (i.e., $\chi^2_\nu \sim 1$) with the smallest number of free parameters. The uncertainty comes from the fact that this high-energy component was observed over a narrow energy range between 100 and 300 keV (due to the limited sensitivity above ~ 300 keV), and it can be characterized by different models depending on one’s choice.

C. Event C: Transition from plasma-sheet to tail-lobe reconnection

Figure 6 shows an overview of event C with the time series of parameters, demonstrating a transition from the plasma-sheet reconnection to the tail-lobe reconnection. Observations are shown for 14:12–15:40 UT of July 17, 2017 and the time periods of plasma-sheet and tail-lobe reconnection are highlighted in yellow and cyan, respectively. At the beginning of the event, the AE index was low (~ 500 nT), but it increased steadily starting at 14:37 UT when MMS detected tailward flows ($V_x < 0$). There was a correlated V_x and B_z reversal at around 14:44 UT (not shown), indicating a passage of the X-line by the spacecraft. The density remained high between 0.1 and 0.3 cm^{-3} [Fig. 6(g)] and the temperature was steady [Fig. 6(i)]. These features are similar to those of event A. However, at around 15:00 UT, the electron temperature started to increase exponentially while the density decreased. By 15:05 UT, the density dropped down to $\sim 0.02 \text{ cm}^{-3}$



Event B

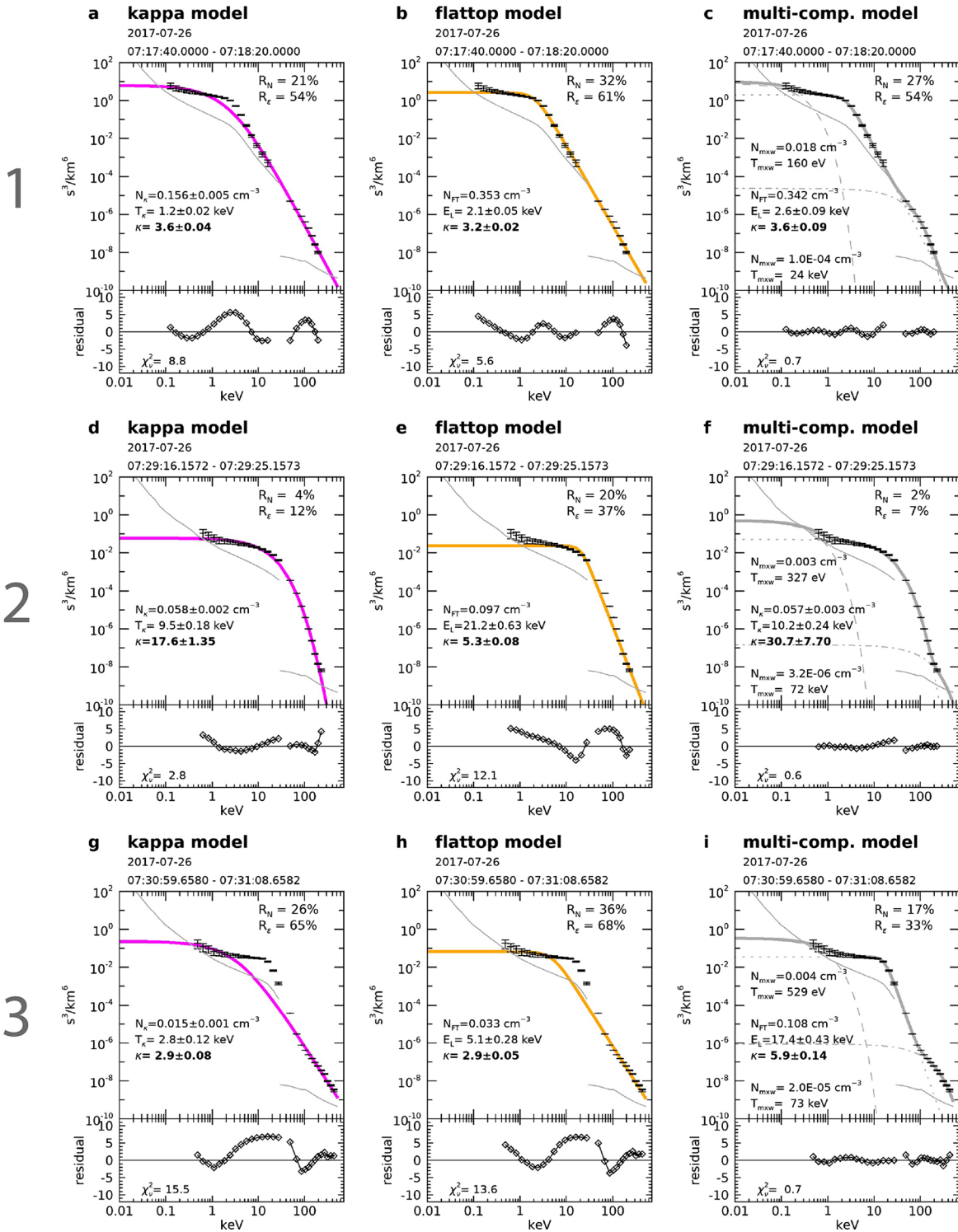


FIG. 5. Example analyses of electron energy spectra obtained in event B (July 26, 2017). The format is the same as Fig. 3.

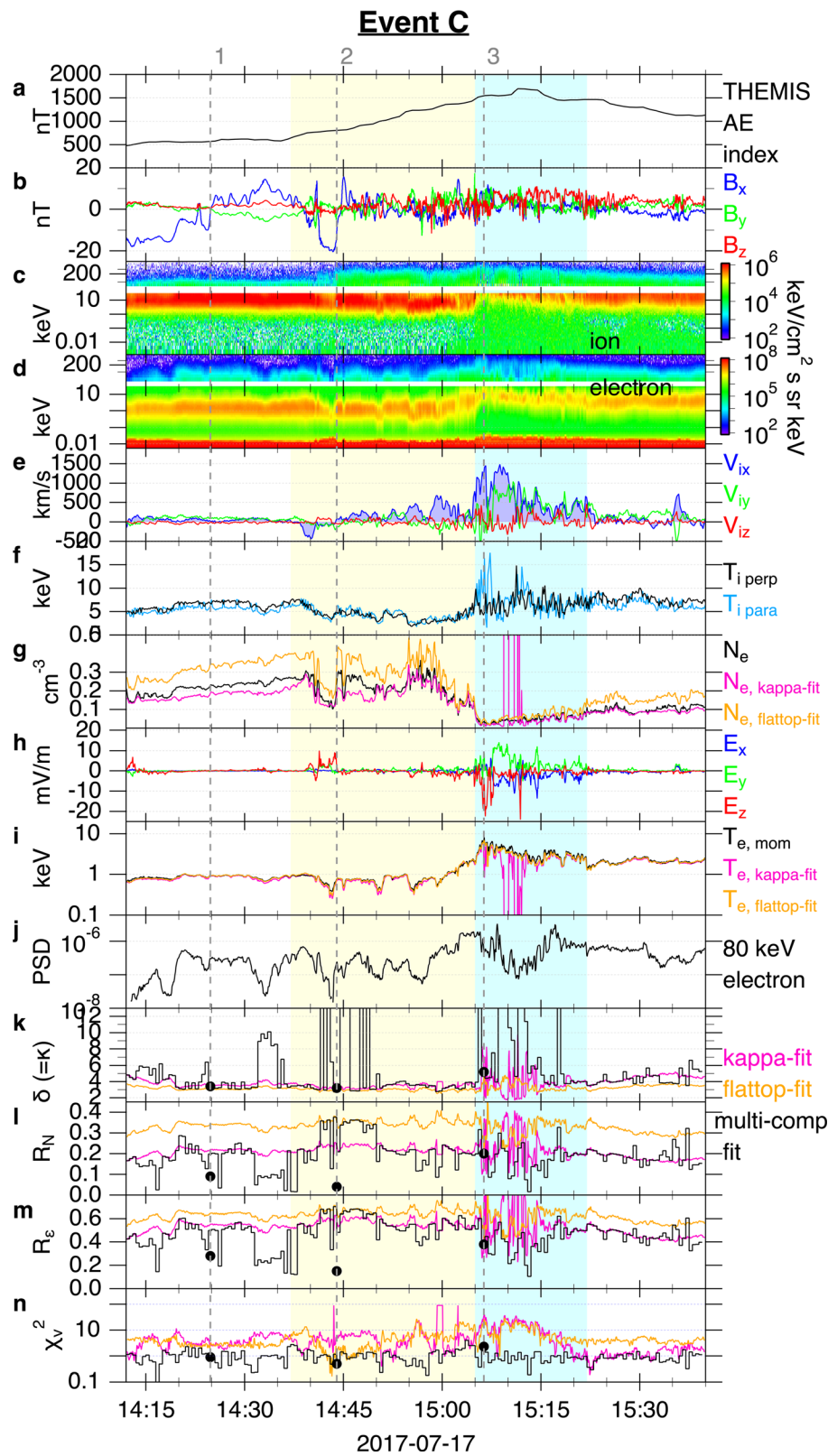


FIG. 6. Overview of event C (July 17, 2017), demonstrating two different phases of reconnection. The format is the same as Fig. 2 except that two different time periods of reconnection, one for event-A-like and another for event-B-like, are highlighted in light yellow and light blue, respectively. The vertical dashed lines indicate the times of energy spectra shown in Fig. 7.

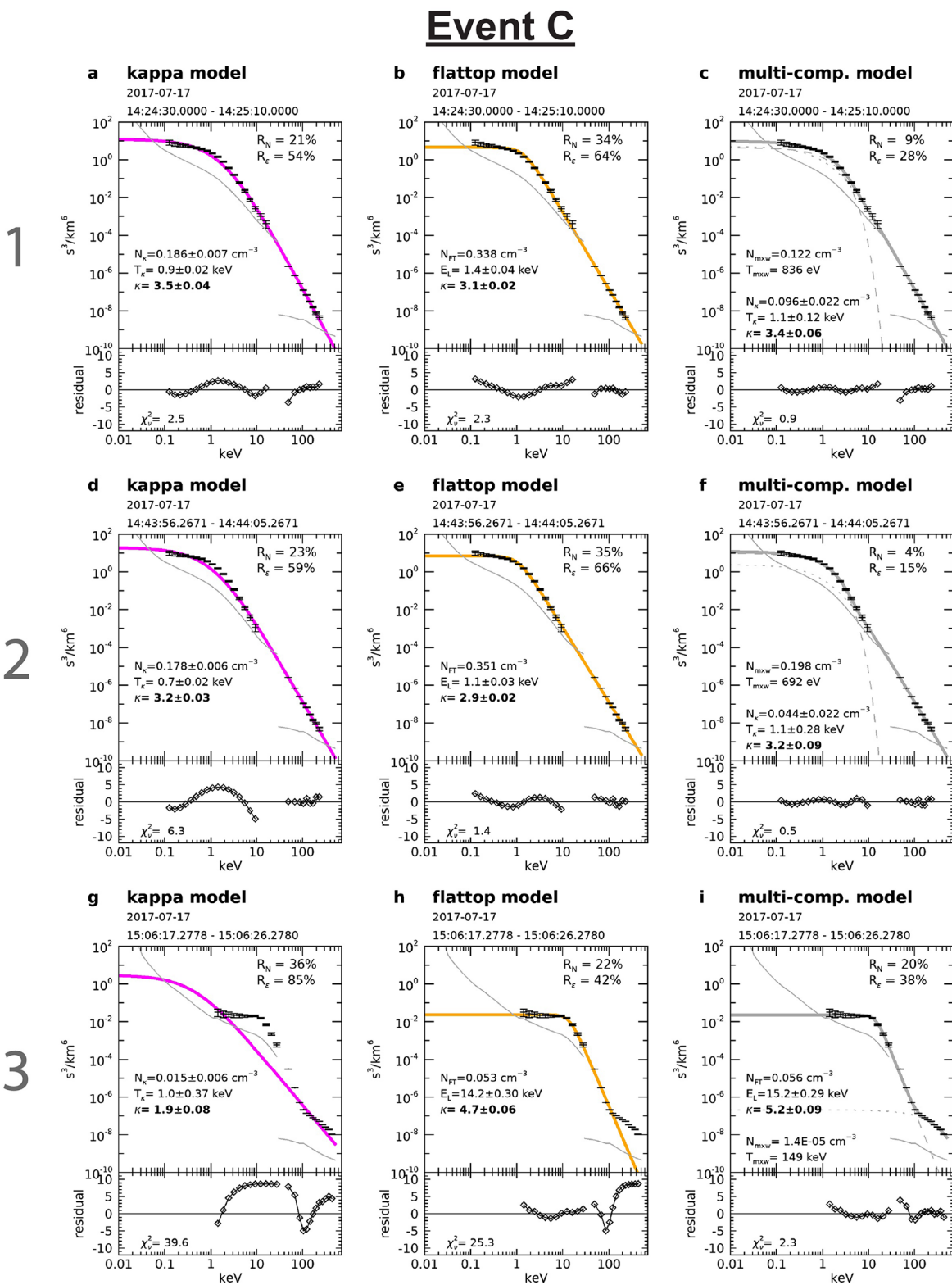


FIG. 7. Example analyses of electron energy spectra in event C (July 17, 2017). The format is the same as Fig. 3.

and the ion flow speeds increased to ~ 1500 km/s, and the electron temperature increased up to ~ 10 keV, all of which suggest enhanced reconnection and energization of particles.

The observed evolution is consistent with our interpretation that plasma-sheet reconnection occurred first and then tail-lobe reconnection followed. Once the pre-existing populations are pushed away from the reconnection region, the energy release became more explosive. As for energetic particles, energetic ion flux enhanced at the beginning of the plasma-sheet reconnection [$\sim 14:45$ UT, Fig. 6(c)] and remained steady, whereas ~ 80 keV electron flux were already high ($\sim 3 \times 10^{-7}$ s 3 /km 6) before the event and remained high throughout the event [Figs. 6(d) and 6(j)].

Figure 7 shows three example energy spectra, demonstrating basically the same features that were observed in events A and B. While the kappa distribution can generally represent the spectrum (a) and (d), an additional population is necessary to improve the fit (c) and (f). Using the flattop distribution instead of the kappa distribution also improves the fit sometimes [compare between (d) and (e) and between (g) and (h)]. Therefore, sometimes, different models can fit the data equally well, leading to the ambiguity of the non-thermal fraction of electron energies [compare between (e) and (f)]. Regarding the time evolution, the spectrum was already hard before the reconnection (spectrum 1) and the flattop distribution appeared intermittently during the tail-lobe reconnection phase (spectrum 3).

D. Average electron energy and electric field magnitude

Spectrum 2 of event B [Fig. 5(f)] clearly indicates that the non-thermal component can be small ($\sim 7\%$) when the temperature is high (~ 10 keV as opposed to the typical temperature in the plasma sheet ~ 1 keV). To better understand how reconnection controls electron energization (both heating and non-thermal acceleration), we examined the $|-V_e \times B|$ electric field, where V_e is the electron bulk flow speed, the average energy of electrons $\bar{\epsilon}$, and the non-thermal fraction of electron energies R_e as a function of local electric field magnitude $|E|$, as shown in Fig. 8. Here, we use all three events and the data are averaged over 30 s, and the spectral fitting results are used to derive $\bar{\epsilon}$.

The spectral fitting results are also shown as stepped lines in Figs. 2, 4, and 6. If a multi-component model is used to fit the data, we averaged the values of $\bar{\epsilon}$ from all components.

Figure 8(a) shows clearly that $|E|$ is correlated with the predicted value from $-V_e \times B$, indicating that the electric fields are properly measured and can be used for further analysis. The correlation coefficient of 0.62 is relatively low because of the scattering of the data points for event B (cyan). Events A and C produce the correlation coefficient of 0.96 and 0.98, respectively.

Figure 8(b) shows $\bar{\epsilon}$ is correlated with $|E|$. As annotated in the figure, the correlation coefficient is 0.78. It is to be emphasized that the electron temperature remained steady across event A and the earlier phase of event C. This is a noticeable feature of the plasma-sheet reconnection, as described in Secs. IV A–IV C. With the data points from event A only (colored dark yellow), the correlation coefficient is -0.45 (not annotated), meaning that there is no correlation. On the other hand, with the data points from event B only (colored cyan), the correlation coefficient is 0.65 (not annotated), meaning that there is a modest correlation between $|E|$ and $\bar{\epsilon}$, in event A.

Figure 8(c) shows $\bar{\epsilon}$ from the non-thermal component alone. The correlation is weaker but there is a tendency that a higher value of $|E|$ leads to a higher value of $\bar{\epsilon}$. However, the non-thermal fraction R_e does not show a clear correlation with $|E|$, as shown in Fig. 8(d). It is clear from the scatterplot that the non-thermal fraction can be small even when the electric field is large, and the average electron energy (or the temperature) is also large. In fact, the correlation coefficient was negative, -0.38 , suggesting anti-correlation.

In principle, the average electron energy $\bar{\epsilon}$ can also be estimated from the electron temperature T_e (provided by the instrument team) by $\bar{\epsilon} = (3/2)k_B T_e$ and is shown in Fig. 8(b) in gray. For the data points from event B (squares), especially those above 6 keV, there is a large deviation between $\bar{\epsilon}$ derived from spectral fitting (cyan squares) and $\bar{\epsilon}$ derived from the electron moment (black plus signs). When the temperature is high, the entire energy distribution shifts toward the higher energies and a significant part can extend past the detection limit of the FPI instrument. Thus, in such cases, the moment calculation, which is based on the FPI instrument only, overestimates the temperature.

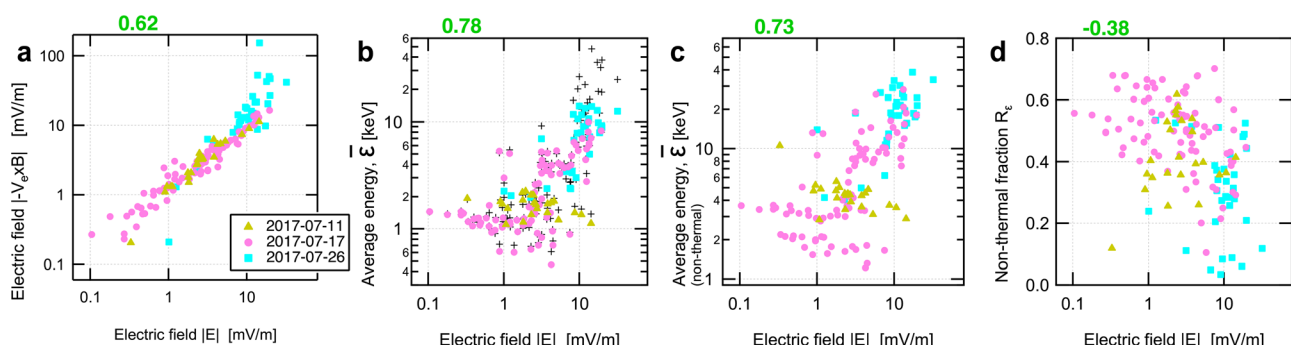


FIG. 8. Comparison between electric field magnitude $|E|$ and four different parameters: (a) the electric field calculated from $|-V_e \times B|$, (b) average energy of electrons $\bar{\epsilon}$, (c) the same as (b) but for non-thermal electrons, and (d) non-thermal fraction of electron energy R_e . The data points are obtained by averaging the data over 30 s and by applying spectral fitting for each averaged data. The black plus signs in panel (b) are obtained from the FPI electron moment data. Correlation coefficients are annotated on the upper left corners.

Figure 9 shows comparisons between $|E|$ and T_e (equivalent to \bar{e}) obtained from the moment data but at a higher sampling rate, 4.5 s. It is more clearly demonstrated that, in plasma-sheet reconnection events, T_e was almost constant at ~ 1 keV and was not sensitive to $|E|$. On the other hand, in the tail-lobe reconnection events, the data points are more scattered and the correlation between T_e and $|E|$ is less clear when compared to Figs. 8(b) and 8(c). This is partly due to the artifact described above. Nevertheless, it is evident that both T_e and $|E|$ were substantially higher than those in the plasma sheet reconnection.

V. SUMMARY AND DISCUSSION

We here summarize the main observed features in the electron energy spectra in earth's magnetotail, followed by a detailed discussion of some specific features.

1. The electron energy spectra in earth's magnetotail are often represented by the kappa distribution in both cases of plasma-sheet and tail-lobe reconnection, and the power-law index $\delta (= \kappa)$ becomes as small as 3–4. However, the flattop distribution sometimes represents the core component better than the kappa distribution. Also, an additional thermal population is often necessary to better fit the data over the entire energy range, suggesting a presence of at least one additional population of electrons in the plasma sheet. It can be a cold population in the very low energy range or a hot population at very high energy. Sometimes, there can be both.
2. Because of the variations in the energy spectrum, our estimation of the non-thermal fraction also varied greatly between 20% and 60% in the active reconnection region. A complication is that, in some cases, different spectral models can fit the same data equally well but the derived non-thermal fraction differs because of the difference in the models. Furthermore, the derived non-thermal fraction varies greatly from sample to sample, even if the same one model fits the data better than any other models. These effects lead to the large variation (or uncertainty) in the estimation of the non-thermal fraction.
3. During the tail-lobe reconnection, the non-thermal tail is less enhanced even when the electric field is large and the temperature is also large. In other words, the non-thermal fraction R_e is not correlated with $|E|$. However, the average energy of electrons (or equivalently temperature) is linearly correlated with the electric field magnitude during the tail-lobe reconnection, indicating that the electric field fluctuations plays an important role in energizing electrons (especially heating).

A. Plasma-sheet reconnection vs tail-lobe reconnection

Our observations are well consistent with the classical picture of plasma-sheet reconnection and tail-lobe reconnection. We demonstrated that the $T_e - |E|$ plot is an easy way to diagnose and visualize the two different regimes in one panel, although there can be artificial overestimation of temperature for the cases of tail-lobe reconnection (Fig. 9). In the plasma-sheet reconnection, the electron temperature remains largely unchanged. In addition to events A, B, and C, we examined a few other cases of plasma-sheet reconnection and found the same trend, although the temperature is not always centered

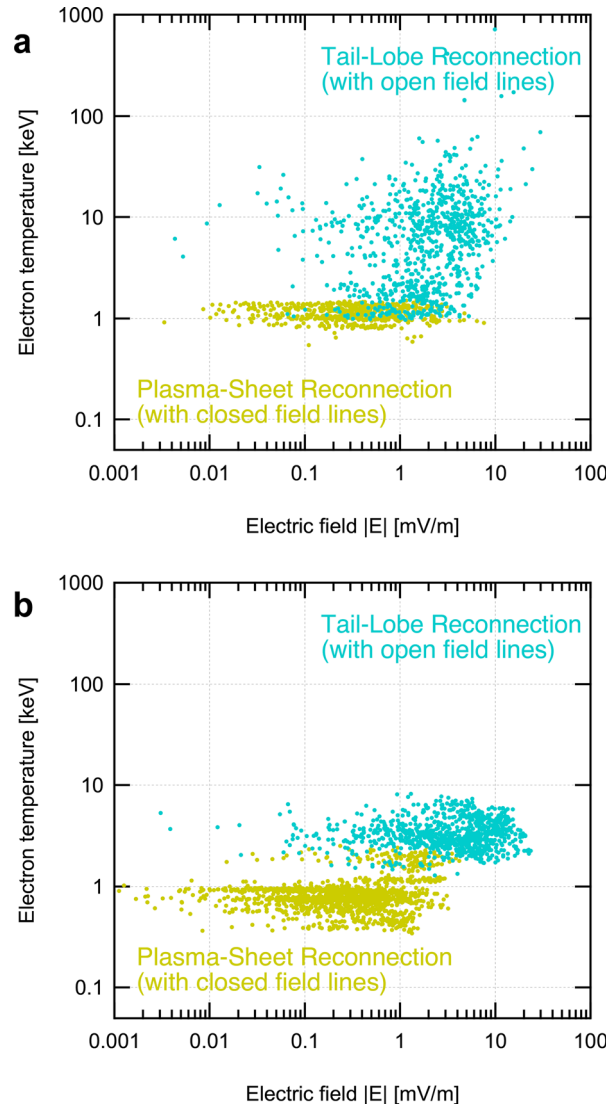


FIG. 9. Classification of tail-lobe and plasma-sheet reconnection in the electron temperature T_e vs electric field magnitude $|E|$ map. Panel (a) shows the data points from event A (July 11, 2017 dark yellow) and event B (July 26, 2017 cyan). Panel (b) shows data points from event C only (July 17, 2017) but colored differently for the two phases of reconnection, i.e., plasma sheet reconnection (dark yellow) and tail lobe reconnection (cyan). All data points in both panels are taken from the active reconnection region, as highlighted in yellow and cyan in Figs. 2, 4, and 6. T_e is taken from the FPI moment data at 4.5 s sampling time, as shown in panel (i) of Figs. 2, 4, and 6. The high values of T_e (especially those above 10 keV) may be a result of overestimation (see texts). The electric field was measured by EDP and are averaged over the same 4.5 s periods. The original data before averaging are shown in panel (h) of Figs. 2, 4, and 6.

around 1–2 keV. For example, in the event on July 3, 2017 at around 05:26 UT, T_e was steady around ~ 0.1 keV rather than 1–2 keV (Chen *et al.*, 2019b). Therefore, we consider that the steadiness of the temperature is not artificial.

We think that the temperature remains steady in the plasma-sheet reconnection because the Alfvén speed V_A remains small. As described in Sec. I, a smaller V_A leads to a smaller increase in electron energy (or temperature). Thus, if the temperature increase was much smaller than the initial temperature of the preexisting plasma sheet, the increase would be unnoticeable.

When compared between the tail-lobe reconnection and plasma-sheet reconnection, the average electron energy increased by an order of magnitude (Fig. 8). This can be interpreted by Eq. (1). Here, we assume that the factor $C \equiv \alpha_R(L/d_i)$ is constant. This is not too unrealistic because statistical studies from the magnetopause reconnection show C is in fact nearly constant and $C \sim 0.017$ (e.g., Phan *et al.*, 2013). For the tail-lobe reconnection in event B, B_x was at most ~ 22 nT and N was ~ 0.03 cm $^{-3}$ when the temperature was high (07:27–07:39 UT). Thus, we estimate $V_A \sim 2800$ km/s. For the plasma-sheet reconnection in event A, B_x was at most ~ 15 nT and N was ~ 0.1 cm $^{-3}$. Thus, we estimate $V_A \sim 1040$ km/s. These estimate indicates that V_A^2 differed by a factor of ~ 7 , which can marginally explain an order of magnitude difference of the electron average energy between the two events. For event C during which reconnection transitioned from the plasma-sheet reconnection phase to the tail-lobe reconnection phase, we consider a constant $B_x \sim 20$ nT but a density decrease from 0.25 to 0.03 cm $^{-3}$. This corresponds to a change of V_A from ~ 880 to ~ 2540 km/s and a change of V_A^2 by a factor of ~ 8 , which can again explain an order of magnitude difference of the electron average energy between the two phases.

B. Quiet-time spectra

Christon *et al.* (1989) already reported that electrons exhibit the kappa distribution, i.e., a non-thermal energy spectrum, even in undisturbed ($AE < 100$ nT) geomagnetic conditions with the power-law index of κ in the range of 4–8, with a most probable value between 5 and 6. In this study, we examined the electron energy spectra in the context of reconnection. We found that the non-thermal power-law tail can indeed exist even outside the reconnection region (or, more precisely, the Hall region). Spectrum 1 of both events B and C clearly shows that, even at the current sheet center where $B_x \sim 0$, the spectrum exhibit a hard power-law outside the reconnection region and the power-law index of κ was in the range of 3.4 and 3.6. However, the non-thermal component was much less enhanced ($\kappa > 10$) outside the reconnection region in event A, and the AE index (≤ 100 nT) was substantially smaller than that of events B and C (≥ 500 nT). Therefore, we still think there is a possibility that the presence of the non-thermal tail outside the reconnection region is correlated with the magnetotail activity level (i.e., AE index). We conjecture that the non-thermal tail in the non-reconnecting plasma sheet could be a remnant of previous magnetotail activity. It could also be a leakage from the reconnection region where high-energy electrons are produced. In event A, the power law index increased gradually with the increasing distance from the X-line where it reached a minimum. Also, the energetic electron flux showed an exponential decrease after the passage of the reconnection region. Thus, there could have been a spatial diffusion process, although the decaying profile was not evident in events B and C.

C. Flattop distribution

As described in Sec. II, the flattop distribution has been observed at various locations in earth's plasma environment. Based on our experience of studying several MMS events, we have an impression that the flattop distribution is found more frequently in tail-lobe reconnection and is associated with fast, heated plasmas in the exhaust region. However, we did not study those reconnection-associated, fine-scale structures in detail. Here, we note that, in our events, the shoulder energy of the flattop distribution was very high and it often reached ≥ 15 keV [Figs. 5(i) and 7(i)]. This energy is much higher than the typical value of ≤ 4 keV in earlier reports, although Chen *et al.* (2009) reported the shoulder energy of ~ 10 keV.

D. High-energy component

During the enhanced, tail-lobe reconnection, we often observed an additional high-energy spectral component in the >100 keV range (See spectrum 3 of events B and C). This component was fitted by the Maxwellian distribution with unrealistically high temperature (~ 66 keV) just to avoid over-fitting. It is possible that this high-energy component has a power-law form (See Sec. IVB for more details). Regarding the origin of this high-energy component, we noticed that it is sometimes associated with a parallel anisotropy and evolves gradually into a single kappa distribution with no spectral break between the core and high-energy components. Thus, we have an impression that this high-energy component is a population escaping from the energization site where the kappa distribution is formed. However, more detailed analysis and conclusive discussion are left for future work.

E. Maximum attainable energy

Our observations show that the electron energy spectra can extend up to >430 keV within the reconnection region (Figs. 5 and 7). This is consistent with earlier reports of high-energy electrons. For example, Terasawa and Nishida (1976) and Baker and Stone (1976) found >500 keV and >200 keV electrons, respectively, at and around the reconnection region. Also, Øieroset *et al.* (2002) studied >300 keV electrons across the ion-scale diffusion region. Here, we note that, while we sometimes find an enhanced flux at a higher energy that can be modeled by an exponential curve (or Maxwellian) [for example, see Fig. 5(i)], we did not find a power-law tail that smoothly falls off at a certain energy, as they hit the detection limit. Therefore, the maximum energy attainable in the magnetotail reconnection region (or the upper-limit of the electron power-law tail) remains unclear.

It is to be emphasized that such high-energy electrons in earth's magnetotail are difficult to explain with the classical idea of electron acceleration by the coherent, cross-tail DC electric field (or potential drop). At the global scale, the cross-tail potential can actually be inferred from the polar cap potential Φ_{PC} . It is derived from measuring the convection flows in the high-latitude ionosphere and is typically <200 kV (e.g., Shepherd, 2007). Thus, the induced electric field across the magnetotail can explain electron energization only up to ~ 200 keV.

One may argue that the reconnection electric field can be enhanced locally in the magnetotail. Unfortunately, it is difficult to accurately measure the reconnection electric field (e.g., Genestreti *et al.*, 2018). Assuming the reconnection rate $\alpha_R = 0.1$, density $N = 0.1$ cm $^{-3}$, and the magnetic field $B_x = 10$ nT, Terasawa and

Nishida (1976) argued that the reconnection electric field $E_R = \alpha_R V_A B_x$ should be 0.6 mV/m or 4 kV/R_E and that it is not enough to explain the high-energy (>500 keV) electrons.

While the magnetotail width is typically $\sim 40 R_E$, recent observations and simulations indicate that the reconnection flow channel is quite localized in the dawn-dusk direction (1–2 R_E) and expands gradually after reconnection onset (e.g., Sergeev *et al.*, 1996; Angelopoulos *et al.*, 1996, 1997; Nakamura *et al.*, 2004; Liu *et al.*, 2013; and Pritchett and Lu, 2018). Thus, E_R = 4 kV/R_E can explain electron energy up to only 20 keV for the channel width of L = 5 R_E. If we use N = 0.05 cm⁻³ and the magnetic field B_x = 30 nT, then E_R can be as large as 8.8 mV/m or 56 kV/R_E but it can explain electron energization up to at most 280 keV for L = 5 R_E.

F. Electron energization process

We found that, in the tail-lobe reconnection, the average electron energy $\bar{\varepsilon}$ (or equivalently T_e) is linearly correlated with the locally measured electric field magnitude |E|, as indicated by the cyan marks in Fig. 8. Because the electric field fluctuates greatly and, thus, is likely to be the result of waves and turbulence, the linear correlation suggests that electrons are energized (both heated and accelerated to non-thermal energies) by interacting with the electric field fluctuations. This is favorable for a stochastic Fermi acceleration in waves or turbulence. This is also consistent with the recent study of event B by Ergun *et al.* (2020a; 2020b). They more clearly showed direct evidence of electron energization by electric field fluctuations by analyzing J · E, where J is the electron current and E is the electric field fluctuation. It was concluded that the primary transfer of magnetic energy to particle energy is advanced by large-amplitude electric field structures generated by strong turbulence.

The origin and nature of the electric field turbulence and associated electron energization remain unclear. One reason for this is because, in this study, we focused on the large-scale variations of the electron energy spectra over the entire duration of events using the survey data. More detailed studies in the past have proposed a wide variety of fine-scale, kinetic structures that can potentially provide an energy kick to particles. Examples include, but not limited to, electrostatic solitary waves (e.g., Mozer *et al.*, 2016; Fu *et al.*, 2020, and references therein), magnetic gradient (including dipolarization fronts) (e.g., Hoshino *et al.*, 2001), and magnetic islands (or flux ropes in 3D) (e.g., Drake *et al.*, 2006). See also Birn *et al.* (2012) for a review.

It is to be emphasize that, to explain a formation of the power-law energy spectrum, we likely need the stochastic Fermi process (Fermi, 1949). It is a generalized theory that explains a power-law formation with hypothetical “clouds.” Many of the modern (and specific) theories of particle acceleration is focused on what specific structure can actually play the role of the “clouds” and how the stochasticity can be achieved. Our result in this paper supports this classical idea that a stochastic process is important for energization, but it does not clarify the detailed nature of each energy kick nor the origin of the turbulence needed for the stochasticity.

In fact, the need for turbulence has been discussed more considerably in the past years. Let us consider the well-known contract island mechanism, as an example. Theoretically, a Fermi process can be achieved even in 2D magnetic islands without turbulence (e.g., Drake *et al.*, 2006). In a contracting island, particles can gain energy at each end of the island by drifting in the same out-of-plane direction (not

the in-plane direction). Thus, the particle motion is uni-directional and, therefore, the finite length of the flux tube (or the width across the magnetotail) limits the energy gain, just like the coherent reconnection is difficult to explain the maximum electron energy, as described above. However, if there was a chain of dynamically evolving and merging islands, the reconnection electric can change its direction at the merging point, resulting in bi-directional motion of particles (Oka *et al.*, 2010). This means that the particle energy gain is not limited by the finite length of the flux tube even in 2D configuration.

Nevertheless, additional turbulent scattering is required to explain the power-law formation (e.g., Drake *et al.*, 2006). Also, it is not clear from observations how many flux ropes are there in earth’s magnetotail, although waves and turbulence have been observed frequently. While a variety of kinetic scale processes has been explored in the context of anomalous resistivity, the observed properties of the electric field turbulence appear to be consistent with the lower hybrid drift instability (LHDI) (e.g., Cattell and Mozer, 1986; Shinohara *et al.*, 1998). Recent particle simulations have also indicated that the presence of an ambient guide field would lead to more enhanced turbulence through the generation of small-scale, magnetic islands along the separatrices (e.g., Daughton *et al.*, 2011). Thus, reconnection becomes intrinsically turbulent in a 3D system. A key point here is that, when reconnection becomes turbulent, particles move more chaotically and are more likely to experience a stochastic Fermi process (e.g., Dahlin *et al.*, 2015; Li *et al.*, 2019). While Ergun *et al.* (2020a; 2020b) suggested the importance of electron-scale magnetic depletion that appear in association with the turbulence, it would be desirable to have a more detailed study of the enhanced turbulence and associated electron acceleration from both observation and simulation points of view.

G. What parameters control the energization?

From our observational results as well as the discussion presented above, we conclude that

1. the large-scale variation of energization (i.e., plasmas-sheet and tail-lobe reconnection) depends on V_A²; and
2. the locally measured variation of energization (i.e., the average energy $\bar{\varepsilon}$) depends on the instantaneous electric field magnitude |E|.

In other words, V_A² represents the global effect, whereas |E| represents the local effect, but the physical connection between two remains unclear. We provided an idea that the reconnection electric field E_R might be playing a role [Sec. I, Eq. (1)], but it is not tested in this study.

There are actually many other parameters that can potentially affect electron energization during reconnection (e.g., Imada *et al.*, 2011; Zhou *et al.*, 2016). Examples include the current sheet thickness, the in-plane Hall electric field (E_N), ion-to-electron temperature ratio, the reconnection rate, and the outflow speeds. Imada *et al.* (2011) showed that the ion heating, electron heating, current sheet thickness, reconnection electric field, and converging normal electric field E_N show good correlation with the electron acceleration efficiency. Zhou *et al.* (2016) showed electron acceleration is positively correlated with outflow speeds and the power-law index.

While these studies focused on the non-thermal component alone, Phan *et al.* (2013) analyzed many reconnection events statistically and found a very large correlation coefficient (0.94) between ΔT_e

and $m_i V_A^2$, where ΔT_e is derived from the moment and thus includes the non-thermal component. Such a high correlation indicates that V_A^2 is a very important parameter for controlling electron energization during reconnection. Our result that V_A^2 can explain the overall difference between the plasma-sheet and tail-lobe reconnection is qualitatively consistent with the statistical result by Phan *et al.* (2013). However, the fact that the non-thermal component can be small even when the temperature is high or the local electric field is large (Fig. 8) remains as a puzzle and needs to be studied further.

H. Non-thermal fraction of electron energies

Our spectral analysis indicates that the non-thermal fraction of electron energies R_e during reconnection varied between 20% and 60% when the data are reasonably well fit. A puzzle is that it can be small even when the electric field is large and the temperature is also large [e.g., Fig. 5(f)]. This does not mean electrons are not energized. Electrons do gain a substantial amount of energy but they do not always form a power-law. In such cases, we think that the heating process was more dominant than the process of power-law formation.

Interestingly, similar values of R_e have been obtained for the above-the-looptop (ALT) hard x-ray coronal sources in solar flares. In solar flares, the possible reconnection region in the corona does not produce a detectable amount of hard x rays, which is probably because of the rather low coronal density and correspondingly low probability of bremsstrahlung emission. Thus, a nearby x-ray source, the so-called above-the-looptop (ALT) hard x-ray source, has drawn a considerable attention (e.g., Masuda *et al.*, 1994; Krucker *et al.*, 2010). Generally, it is considered to correspond to the collapsing region in earth's magnetotail, where the magnetic field lines become more dipolarized and the so-called flow braking and/or current disruption have been observed (compare, for example, Figs. 4 and 8 of Oka *et al.*, 2018). Unfortunately, the measurements of the ALT x-ray spectra in the thermal energy range (typically below ~ 10 keV) have not been well constrained due to the limited dynamic range of the x-ray telescopes. However, based on supplementary material from x-ray imaging-spectroscopy as well as the differential emission measure (DEM) of the extreme-ultraviolet (EUV) wavelength data, it has been suggested that the kappa distribution can also explain the x-ray spectra in the ALT source (Oka *et al.*, 2013; 2015). Combined with another case study (Battaglia *et al.*, 2015), a total of six different cases of ALT observations have been analyzed with the kappa distribution model and the obtained power-law index κ was in the range of 3.8–14, implying the non-thermal fraction of electron energies of $R_e = 16\%-52\%$. Here, the x-ray spectra were integrated over a >30 s time period, centered around one of the impulsive x-ray peaks detected in a flare that typically lasted 5–10 min.

A caveat is that the origin of the variation of R_e is different in solar flares and the magnetotail. In the magnetotail, the variation came from the deviations from the kappa distribution model. Note that the plasma is basically collisionless in earth's magnetotail. Also, our observations were focused on the reconnection region (more precisely, the Hall region) rather than the collapsing region. In contrast, the same, single kappa distribution model was used in all six cases of solar flare ALT observations, and the variation of the κ values has been attributed to the different densities, and, hence, the rate of collisions, in the ALT region. In fact, it has been argued that, when the density is high in the (above-the-)looptop region, the power-law spectrum becomes soft and

the accelerated electrons lose their energies in the corona (i.e., the so-called coronal thick-target events) (e.g., Veronig and Brown, 2004).

Despite significant differences in the plasma environments, it is interesting that both solar flares and earth's magnetotail produce a similar range of the power-law index κ and the resultant non-thermal fraction of electron energies R_e . While such a similarity of the power-law index has been suggested in the past (e.g., Oka *et al.*, 2018), we envision that a detailed spectral analysis such as the one presented in this study would facilitate more comparative studies of particle acceleration during explosive energy-release in solar and terrestrial plasma environments.

ACKNOWLEDGMENTS

We thank all members of the MMS project. This work was supported by NASA under Grant Nos. 80NSSC18K1002, 80NSSC18K1373, and 80NSSC20K0627 at UC Berkeley.

AUTHOR DECLARATIONS

Conflict of Interest

The authors have no conflicts to disclose.

DATA AVAILABILITY

The data that support the findings of this study are openly available in MMS Science Data Center at <https://lasp.colorado.edu/mms/sdc/public/>, Baker *et al.*, 2016.

APPENDIX A: DATA MASKING

For spectral analysis, we removed (or masked) data points that are affected by artificial effect including photoelectrons. While the spacecraft potential generally gives a good indication of the upper limit of the energies of photoelectrons, it appears to be a rough estimate. A photo-electron model can be used to remove such data points more accurately (Gershman *et al.*, 2017), but the model is not always available. To ensure the removal of photoelectrons, we only use data points in the >100 eV range. This criterion simplifies our analysis and yet it still allows us to perform reasonable spectral fitting of the main plasma populations in the plasma sheet, as shown in Sec. IV. A caveat is that we might be removing real signals from a possible cold population. A diagnosis of such a low temperature plasma requires a more careful analysis and left for future work.

Another complication is that the electron energy spectrum can reach the detection limit (i.e., one-count-level) and becomes noisy not only in the higher energy range but also in the lower energy range. It can occur if the density is low and temperature is high and if there is no additional cold population. Thus, prior to each spectral fitting, we calculated the energy E_1 at which the observed phase space density becomes closest to the detection limit. Then, we removed all data points at energies smaller than E_1 . Note that, under typical conditions, the data are not noisy and the flux is substantially high in the $E < E_1$ range due to the presence of photoelectrons. Thus, in some cases, E_1 could also be regarded as the boundary between photoelectrons and real plasma data. However, it can sometimes be confounded by the possible cold population described above.

To summarize, we removed data points in the energy range below E_1 or E_2 ($=100$ eV) whichever is higher. E_1 is less than 1 keV in many cases. Also, in the higher energy range of each instrument (typically >10 keV and >100 keV for FPI and FEEPS, respectively), data points are removed if the flux were comparable to the detection limit.

APPENDIX B: MODEL FITTING

To fit the spectral data, we used a nonlinear least squares method with an IDL routine mpfit (Markwardt, 2009). For the initial values, the observed moment values (density and temperature) are used for the main spectral component. Because the bulk flow speed is much less than electron thermal velocity, we assumed an isotropic distribution of electrons and did not use flow velocity in the moment data. The initial values of the other parameters, including the power-law index, were empirically determined although they were not crucial for the success of the spectral fitting except in rare cases where a cold population existed. It was more important to set weights properly as described below.

In general, the difference between the observation (f_i) and the model (f_{model}) is normalized by the experimental error (Δf_i), where the subscript i represents an energy channel. However, in the case of our study, the several points of the FEEPS data have a much higher count rate than FPI (as can be seen as the much lower one-count-level in the figures presented in this paper), leading to a larger weight on FEEPS data points and thus a failure of the spectral fitting of the entire energy spectrum. To avoid this problem, we redistributed the weights. While the actual, relative error size, $\alpha_i \equiv \Delta f_i / f_i$, can vary by many orders of magnitude depending on the energy channel (i) or instrument, we assumed a uniform value of $\bar{\alpha}$ so that weights w_i can be defined as $w_i \equiv 1/(\bar{\alpha} f_i)^2$. Here, $\bar{\alpha}$ is obtained from the average of the actual values of $\Delta f_i / f_i$ so that the reduced chi-square (χ^2_ν) still represents the deviation normalized by the measurement error and that it approaches to unity in the case of a reasonably good fit.

REFERENCES

- Andrae, R., Schulze-Hartung, T., and Melchior, P., arXiv:1012.3754 (2010).
- Angelopoulos, V., Coroniti, F. V., Kennel, C. F., Kivelson, M. G., Walker, R. J., Russell, C. T., McPherron, R. L., Sanchez, E., Meng, C.-I., Baumjohann, W., Reeves, G. D., Belian, R. D., Sato, N., Friis-Christensen, E., Sutcliffe, P. R., Yumoto, K., and Harris, T., *J. Geophys. Res.: Space Phys.* **101**, 4967, https://doi.org/10.1029/95JA02722 (1996).
- Angelopoulos, V., Phan, T. D., Larson, D. E., Mozer, F. S., Lin, R. P., Tsuruda, K., Hayakawa, H., Mukai, T., Kokubun, S., Yamamoto, T., Williams, D. J., McEntire, R. W., Lepping, R. P., Parks, G. K., Brittnacher, M., Germany, G., Spann, J., Singer, H. J., and Yumoto, K., *Geophys. Res. Lett.* **24**, 2271, https://doi.org/10.1029/97GL02355 (1997).
- Asano, Y., Nakamura, R., Shinohara, I., Fujimoto, M., Takada, T., Baumjohann, W., Owen, C. J., Fazakerley, A. N., Runov, A., Nagai, T., Lucek, E. A., and Rème, H., *J. Geophys. Res.: Space Phys.* **113**, A01207, https://doi.org/10.1029/2007JA012461 (2008).
- Asano, Y., Shinohara, I., Retinò, A., Daly, P. W., Kronberg, E. A., Takada, T., Nakamura, R., Khotyaintsev, Y. V., Vaivads, A., Nagai, T., Baumjohann, W., Fazakerley, A. N., Owen, C. J., Miyashita, Y., Lucek, E. A., and Rème, H., *J. Geophys. Res.: Space Phys.* **115**, A05215, https://doi.org/10.1029/2009JA014587 (2010).
- Aschwanden, M. J., Caspi, A., Cohen, C. M. S., Holman, G., Jing, J., Kretzschmar, M., Kontar, E. P., McTiernan, J. M., Mewaldt, R. A., O'Flannagain, A., Richardson, I. G., Ryan, D., Warren, H. P., and Xu, Y., *Astrophys. J.* **836**, 17 (2017).
- Baker, D. N., Peterson, W. K., Eriksson, S., Li, X., Blake, J. B., Burch, J. L., Daly, P. W., Dunlop, M. W., Korth, A., Donovan, E., Friedel, R., Fritz, T. A., Frey, H. U., Mende, S. B., Roeder, J., and Singer, H. J., *Geophys. Res. Lett.* **29**, 43, https://doi.org/10.1029/2002GL015539 (2002).
- Baker, D. N., Riesberg, L., Pankratz, C. K., Panneton, R. S., Giles, B. L., Wilder, F. D., and Ergun, R. E., *Space Sci. Rev.* **199**, 545 (2016).
- Baker, D. N. and Stone, E. C., *Geophys. Res. Lett.* **3**, 557, https://doi.org/10.1029/GL0031009p00557 (1976).
- Battaglia, M., Motorina, G., and Kontar, E. P., *Astrophys. J.* **815**, 73 (2015).
- Bian, N. H., Emslie, A. G., Stackhouse, D. J., and Kontar, E. P., *Astrophys. J.* **796**, 142 (2014).
- Birn, J., Artemev, A. V., Baker, D. N., Echim, M., Hoshino, M., and Zelenyi, L. M., *Space Sci. Rev.* **173**, 49 (2012).
- Birn, J., Runov, A., and Hesse, M., *J. Geophys. Res.: Space Phys.* **119**, 3604, https://doi.org/10.1002/2013JA019738 (2014).
- Blake, J. B., Mauk, B. H., Baker, D. N., Carranza, P., Clemmons, J. H., Craft, J., Crain, W. R., Crew, A., Dotan, Y., Fennell, J. F., Friedel, R. H., Friesen, L. M., Fuentes, F., Galvan, R., Ibscher, C., Jaynes, A., Katz, N., Lalic, M., Lin, A. Y., Mabry, D. M., Nguyen, T., Pancratz, C., Redding, M., Reeves, G. D., Smith, S., Spence, H. E., and Westlake, J., *Space Sci. Rev.* **199**, 309 (2016).
- Burch, J. L., Dokgo, K., Hwang, K. J., Torbert, R. B., Graham, D. B., Webster, J. M., Ergun, R. E., Giles, B. L., Allen, R. C., Chen, L. J., Wang, S., Genestreti, K. J., Russell, C. T., Strangeway, R. J., and Le Contel, O., *Geophys. Res. Lett.* **46**, 4089, https://doi.org/10.1029/2019GL082471 (2019).
- Burch, J. L., Moore, T. E., Torbert, R. B., and Giles, B. L., *Space Sci. Rev.* **199**, 5 (2016).
- Cao, X., Pu, Z. Y., Zhang, H., Mishin, V. M., Ma, Z. W., Dunlop, M. W., Fu, S. Y., Xie, L., Xiao, C. J., Wang, X. G., Zong, Q. G., Liu, Z. X., Kubyshkina, M. V., Pulkkinen, T. I., Frey, H. U., Korth, A., Fraenz, M., Lucek, E., Carr, C. M., Reme, H., Dandouras, I., Fazakerley, A. N., Reeves, G. D., Friedel, R., Glassmeier, K. H., and Escoubet, C. P., *J. Geophys. Res.: Space Phys.* **113**, A07S25, https://doi.org/10.1029/2007JA012761 (2008).
- Cattell, C. A. and Mozer, F. S., *Geophys. Res. Lett.* **13**, 221, https://doi.org/10.1029/GL013i003p00221 (1986).
- Chen, G., Fu, H. S., Zhang, Y., Li, X., Ge, Y. S., Du, A. M., Liu, C. M., and Xu, Y., *Astrophys. J.* **881**, L8 (2019a).
- Chen, L.-J., Bessho, N., Lefebvre, B., Vaith, H., Asnes, A., Santolik, O., Fazakerley, A., Puhl-Quinn, P., Bhattacharjee, A., Khotyaintsev, Y., Daly, P., and Torbert, R., *Phys. Plasmas* **16**, 056501 (2009).
- Chen, L.-J., Bhattacharjee, A., Puhl-Quinn, P. A., Yang, H., Bessho, N., Imada, S., Mühlbacher, S., Daly, P. W., Lefebvre, B., Khotyaintsev, Y., Vaivads, A., Fazakerley, A., and Georgescu, E., *Nat. Phys.* **4**, 19 (2008).
- Chen, L.-J., Wang, S., Hesse, M., and Ergun, R., *Geophys. Res. Lett.* **46**, 6230, https://doi.org/10.1029/2019GL082393 (2019b).
- Christon, S. P., Mitchell, D. G., Williams, D. J., Frank, L. A., Huang, C. Y., and Eastman, T. E., *J. Geophys. Res.* **93**, 2562, https://doi.org/10.1029/JA093iA04p02562 (1988).
- Christon, S. P., Williams, D. J., Mitchell, D. G., Frank, L. A., and Huang, C. Y., *J. Geophys. Res.* **94**, 13409, https://doi.org/10.1029/JA094iA10p13409 (1989).
- Christon, S. P., Williams, D. J., Mitchell, D. G., Huang, C. Y., and Frank, L. A., *J. Geophys. Res.* **96**, 1 https://doi.org/10.1029/90JA01633 (1991).
- Cohen, I. J., Turner, D. L., Mauk, B. H., Bingham, S. T., Blake, J. B., Fennell, J. F., and Burch, J. L., *Geophys. Res. Lett.* **48**, e90087, https://doi.org/10.1029/2020GL090087 (2021).
- Dahlin, J. T., Drake, J. F., and Swisdak, M., *Phys. Plasmas* **22**, 100704 (2015).
- Daughton, W., Roytershteyn, V., Karimabadi, H., Yin, L., Albright, B. J., Bergen, B., and Bowers, K. J., *Nat. Phys.* **7**, 539 (2011).
- Delzanno, G. L., Borovsky, J. E., Henderson, M. G., Resendiz Lira, P. A., Roytershteyn, V., and Welling, D. T., *J. Atm. Sol.-Terr. Phys.* **220**, 105599 (2021).
- Drake, J. F., Swisdak, M., Che, H., and Shay, M. A., *Nature* **443**, 553 (2006).
- Eastwood, J. P., Phan, T. D., Drake, J. F., Shay, M. A., Borg, A. L., Lavraud, B., and Taylor, M. G. T., *Phys. Rev. Lett.* **110**, 225001 (2013).
- Eastwood, J. P., Phan, T. D., Øieroset, M., and Shay, M. A., *J. Geophys. Res.: Space Phys.* **115**, A08215, https://doi.org/10.1029/2009JA014962 (2010).
- Egedal, J., Fox, W., Katz, N., Porkolab, M., Øieroset, M., Lin, R. P., Daughton, W., and Drake, J. F., *J. Geophys. Res.: Space Phys.* **113**, A12207, https://doi.org/10.1029/2008JA013520 (2008).

- Egedal, J., Lê, A., Katz, N., Chen, L.-J., Lefebvre, B., Daughton, W., and Fazakerley, A., *J. Geophys. Res.: Space Phys.* **115**, A03214, <https://doi.org/10.1029/2009JA014650> (2010).
- Ergun, R. E., Ahmadi, N., Kromyda, L., Schwartz, S. J., Chasapis, A., Hoilijoki, S., Wilder, F. D., Cassak, P. A., Stawarz, J. E., Goodrich, K. A., Turner, D. L., Pucci, F., Pouquet, A., Matthaeus, W. H., Drake, J. F., Hesse, M., Shay, M. A., Torbert, R. B., and Burch, J. L., *Astrophys. J.* **898**, 153 (2020a).
- Ergun, R. E., Ahmadi, N., Kromyda, L., Schwartz, S. J., Chasapis, A., Hoilijoki, S., Wilder, F. D., Stawarz, J. E., Goodrich, K. A., Turner, D. L., Cohen, I. J., Bingham, S. T., Holmes, J. C., Nakamura, R., Pucci, F., Torbert, R. B., Burch, J. L., Lindqvist, P. A., Strangeway, R. J., Le Contel, O., and Giles, B. L., *Astrophys. J.* **898**, 154 (2020b).
- Ergun, R. E., Tucker, S., Westfall, J., Goodrich, K. A., Malaspina, D. M., Summers, D., Wallace, J., Karlsson, M., Mack, J., Brennan, N., Pyke, B., Withnell, P., Torbert, R. B., Macri, J., Rau, D., Dors, I., Needell, J., Lindqvist, P.-A., Olsson, G., and Cully, C. M., *Space Sci. Rev.* **199**, 167 (2016).
- Eriksson, C., Vaivads, A., Alm, L., Graham, D. B., Khotyaintsev, Y. V., and André, M., *Geophys. Res. Lett.* **47**, e2019GL085080, <https://doi.org/10.1029/2019GL085080> (2020).
- Feldman, W. C., Anderson, R. C., Bame, S. J., Gosling, J. T., Zwickl, R. D., and Smith, E. J., *J. Geophys. Res.: Space Phys.* **88**, 9949, <https://doi.org/10.1029/JA088iA12p09949> (1983).
- Feldman, W. C., Bame, S. J., Gary, S. P., Gosling, J. T., McComas, D. J., Thomsen, M. F., Paschmann, G., Sckopke, N., Hoppe, M. M., and Russell, C. T., *Phys. Rev. Lett.* **49**, 199 (1982).
- Fermi, E., *Phys. Rev.* **75**, 1169 (1949).
- Fu, H. S., Chen, F., Chen, Z. Z., Xu, Y., Wang, Z., Liu, Y. Y., Liu, C. M., Khotyaintsev, Y. V., Ergun, R. E., Giles, B. L., and Burch, J. L., *Phys. Rev. Lett.* **124**, 095101 (2020).
- Fu, H. S., Khotyaintsev, Y. V., André, M., and Vaivads, A., *Geophys. Res. Lett.* **38**, L16104, <https://doi.org/10.1029/2011GL048528> (2011).
- Gabrielse, C., Angelopoulos, V., Harris, C., Artemev, A., Kepko, L., and Runov, A., *J. Geophys. Res.: Space Phys.* **122**, 5059, <https://doi.org/10.1002/2017JA023981> (2017).
- Genestreti, K. J., Nakamura, T. K. M., Nakamura, R., Denton, R. E., Torbert, R. B., Burch, J. L., Plaschke, F., Fuselier, S. A., Ergun, R. E., Giles, B. L., and Russell, C. T., *J. Geophys. Res.: Space Phys.* **123**, 9130, <https://doi.org/10.1029/2018JA025711> (2018).
- Gershman, D. J., Avanov, L. A., Boardsen, S. A., Dorelli, J. C., Gliese, U., Barrie, A. C., Schiff, C., Paterson, W. R., Torbert, R. B., Giles, B. L., and Pollock, C. J., *J. Geophys. Res.: Space Phys.* **122**, 11548, <https://doi.org/10.1002/2017JA024518> (2017).
- Hones, E. W. J., *J. Geophys. Res.* **82**, 5633, <https://doi.org/10.1029/JA082i035p05633> (1977).
- Hoshino, M., Mukai, T., Terasawa, T., and Shinohara, I., *J. Geophys. Res.: Space Phys.* **106**, 25979, <https://doi.org/10.1029/2001JA900052> (2001).
- Imada, S., Hirai, M., Hoshino, M., and Mukai, T., *J. Geophys. Res.: Space Phys.* **116**, A08217, <https://doi.org/10.1029/2011JA016576> (2011).
- Jaynes, A. N., Turner, D. L., Wilder, F. D., Osmane, A., Baker, D. N., Blake, J. B., Fennell, J. F., Cohen, I. J., Mauk, B. H., Reeves, G. D., Ergun, R. E., Giles, B. L., Gershman, D. J., Torbert, R. B., and Burch, J. L., *Geophys. Res. Lett.* **43**, 7356, <https://doi.org/10.1002/2016GL069206> (2016).
- Ji, H. and Daughton, W., *Phys. Plasmas* **18**, 111207 (2011).
- Kennel, C. F. and Petschek, H. E., *J. Geophys. Res.* **71**, 1, <https://doi.org/10.1029/JZ071i001p00001> (1966).
- Krucker, S., Hudson, H. S., Glesener, L., White, S. M., Masuda, S., Wuelser, J.-P., and Lin, R. P., *Astrophys. J.* **714**, 1108 (2010).
- Leubner, M. P., *Astrophys. Space Sci.* **282**, 573 (2002).
- Li, X., Guo, F., Li, H., Stanier, A., and Kilian, P., *Astrophys. J.* **884**, 118 (2019).
- Lin, R. P. and Hudson, H. S., *Sol. Phys.* **50**, 153 (1976).
- Lindqvist, P. A., Olsson, G., Torbert, R. B., King, B., Granoff, M., Rau, D., Needell, G., Turco, S., Dors, I., Beckman, P., Macri, J., Frost, C., Salwen, J., Eriksson, A., Åhlén, L., Khotyaintsev, Y. V., Porter, J., Lappalainen, K., Ergun, R. E., Wermeir, W., and Tucker, S., *Space Sci. Rev.* **199**, 137 (2016).
- Liu, J., Angelopoulos, V., Runov, A., and Zhou, X. Z., *J. Geophys. Res.: Space Phys.* **118**, 2000, <https://doi.org/10.1002/jgra.50092> (2013).
- Ma, C.-Y. and Summers, D., *Geophys. Res. Lett.* **25**, 4099, <https://doi.org/10.1029/1998GL900108> (1998).
- Markwardt, C. B., *ASP Conf. Ser.* **411**, 251 (2009).
- Masuda, S., Kosugi, T., Hara, H., Tsuneta, S., and Ogawara, Y., *Nature* **371**, 495 (1994).
- Milovanov, A. V. and Zelenyi, L. M., *Nonlinear Processes Geophys.* **7**, 211 (2000).
- Mozer, F. S., Agapitov, O. A., Artemev, A., Burch, J. L., Ergun, R. E., Giles, B. L., Mourenas, D., Torbert, R. B., Phan, T. D., and Vasko, I., *Phys. Rev. Lett.* **116**, 145101 (2016).
- Nakamura, R., Baumjohann, W., Mouikis, C., Kistler, L. M., Runov, A., Volwerk, M., Asano, Y., Vörös, Z., Zhang, T. L., Klecker, B., Rème, H., and Balogh, A., *Geophys. Res. Lett.* **31**, L09804, <https://doi.org/10.1029/2004GL019558> (2004).
- Nakamura, R., Genestreti, K. J., Nakamura, T., Baumjohann, W., Varsani, A., Nagai, T., Bessho, N., Burch, J. L., Denton, R. E., Eastwood, J. P., Ergun, R. E., Gershman, D. J., Giles, B. L., Hasegawa, H., Hesse, M., Lindqvist, P.-A., Russell, C. T., Stawarz, J. E., Strangeway, R. J., and Torbert, R. B., *J. Geophys. Res.: Space Phys.* **124**, 1173, <https://doi.org/10.1029/2018JA026028> (2019).
- Nakamura, T. K. M., Genestreti, K. J., Liu, Y. H., Nakamura, R., Teh, W. L., Hasegawa, H., Daughton, W., Hesse, M., Torbert, R. B., Burch, J. L., and Giles, B. L., *J. Geophys. Res.: Space Phys.* **123**, 9150, <https://doi.org/10.1029/2018JA025713> (2018).
- Norgren, C., Hesse, M., Graham, D. B., Khotyaintsev, Y. V., Tenfjord, P., Vaivads, A., Steinvall, K., Xu, Y., Gershman, D. J., Lindqvist, P. A., Plaschke, F., and Burch, J. L., *J. Geophys. Res.: Space Phys.* **125**, e27440, <https://doi.org/10.1029/2019JA027440> (2020).
- Øieroset, M., Lin, R. P., Phan, T. D., Larson, D. E., and Bale, S. D., *Phys. Rev. Lett.* **89**, 195001 (2002).
- Oka, M., Birn, J., Battaglia, M., Chaston, C. C., Hatch, S. M., Livadiotis, G., Imada, S., Miyoshi, Y., Kuhar, M., Effenberger, F., Eriksson, E., Khotyaintsev, Y. V., and Retinò, A., *Space Sci. Rev.* **214**, 82 (2018).
- Oka, M., Ishikawa, S., Saint-Hilaire, P., Krucker, S., and Lin, R. P., *Astrophys. J.* **764**, 6 (2013).
- Oka, M., Krucker, S., Hudson, H. S., and Saint-Hilaire, P., *Astrophys. J.* **799**, 129 (2015).
- Oka, M., Phan, T. D., Krucker, S., Fujimoto, M., and Shinohara, I., *Astrophys. J.* **714**, 915 (2010).
- Oka, M., Phan, T. D., Øieroset, M., and Angelopoulos, V., *J. Geophys. Res.: Space Phys.* **121**, 1955, <https://doi.org/10.1002/2015JA022040> (2016).
- Olbert, S., *Physics of the Magnetosphere* (Springer, Netherlands, 1968), p. 641.
- Phan, T. D., Shay, M. A., Gosling, J. T., Fujimoto, M., Drake, J. F., Paschmann, G., Øieroset, M., Eastwood, J. P., and Angelopoulos, V., *Geophys. Res. Lett.* **40**, 4475, <https://doi.org/10.1002/grl.50917> (2013).
- Pollock, C. J., Moore, T., Jacques, A., Burch, J. L., Gliese, U., Saito, Y., Omoto, T., Avanov, L., Barrie, A., Coffey, V., Dorelli, J., Gershman, D., Giles, B., Rosnack, T., Salo, C., Yokota, S., Adrian, M., Aoustin, C., Auletti, C., Aung, S., Bigio, V., Cao, N., Chandler, M., Chornay, D., Christian, K., Clark, G., Collinson, G., Corris, T., De Los Santos, A., Devlin, R., Diaz, T., Dickerson, T., Dickson, C., Diekmann, A., Diggs, F., Duncan, C., Figueira-Vinas, A., Firmian, C., Freeman, M., Galassi, N., Garcia, K., Goodhart, G., Guererro, D., Hageman, J., Hanley, J., Hemminger, E., Holland, M., Hutchins, M., James, T., Jones, W., Kreisler, S., Kujawski, J., Lavu, V., Lobell, J., LeCompte, E., Lukemire, A., MacDonald, E., Mariano, A., Mukai, T., Narayanam, K., Nguyen, Q., Onizuka, M., Paterson, W., Persyn, S., Piepgrass, B., Cheney, F., Rager, A., Raghuram, T., Ramil, A., Reichenthal, L., Rodriguez, H., Rouzaud, J., Rucker, A., Samara, M., Sauvaud, J.-A., Schuster, D., Shappirio, M., Shelton, K., Sher, D., Smith, D., Smith, K., Smith, S., Steinfeld, D., Szymkiewicz, R., Tanimoto, K., Taylor, J., Tucker, C., Tull, K., Uhl, A., Vloet, J., Walpole, P., Weidner, S., White, D., Winkert, G., Yeh, P.-S., and Zeuch, M., *Space Sci. Rev.* **199**, 331 (2016).
- Pritchett, P. L. and Lu, S., *J. Geophys. Res.: Space Phys.* **123**, 2787, <https://doi.org/10.1029/2017JA025094> (2018).
- Retinò, A., Nakamura, R., Vaivads, A., Khotyaintsev, Y., Hayakawa, T., Tanaka, K., Kasahara, S., Fujimoto, M., Shinohara, I., Eastwood, J. P., André, M., Baumjohann, W., Daly, P. W., Kronberg, E. A., and Cornilleau-Wehrlin, N.,

- J. Geophys. Res.: Space Phys. **113**, A12215, <https://doi.org/10.1029/2008JA013511> (2008).
- Russell, C. T., Anderson, B. J., Baumjohann, W., Bromund, K. R., Dearborn, D., Fischer, D., Le, G., Leinweber, H. K., Leneman, D., Magnes, W., Means, J. D., Moldwin, M. B., Nakamura, R., Pierce, D., Plaschke, F., Rowe, K. M., Slavin, J. a., Strangeway, R. J., Torbert, R. B., Hagen, C., Jernej, I., Valavanoglou, A., and Richter, I., *Space Sci. Rev.* **199**, 189 (2016).
- Sergeev, V. A., Angelopoulos, V., Gosling, J. T., Cattell, C. A., and Russell, C. T., *J. Geophys. Res.: Space Phys.* **101**, 10817, <https://doi.org/10.1029/96JA00460> (1996).
- Shay, M. A., Haggerty, C. C., Phan, T. D., Drake, J. F., Cassak, P. A., Wu, P., Oieroset, M., Swisdak, M., and Malakit, K., *Phys. Plasmas* **21**, 122902 (2014).
- Shepherd, S. G., *J. Atmos. Sol.-Terr. Phys.* **69**, 234 (2007).
- Shinohara, I., Nagai, T., Fujimoto, M., Terasawa, T., Mukai, T., Tsuruda, K., and Yamamoto, T., *J. Geophys. Res.: Space Phys.* **103**, 20365, <https://doi.org/10.1029/98JA01104> (1998).
- Teh, W.-L., Nakamura, T., Nakamura, R., and Umeda, T., *J. Geophys. Res.: Space Phys.* **123**, 8122, <https://doi.org/10.1029/2018JA025775> (2018).
- Terasawa, T. and Nishida, A., *Planet. Space Sci.* **24**, 855 (1976).
- Thomsen, M. F., Barr, H. C., Gary, S. P., Feldman, W. C., and Cole, T. E., *J. Geophys. Res.* **88**, 3035, <https://doi.org/10.1029/JA088iA04p03035> (1983).
- Torbert, R. B., Burch, J. L., Phan, T. D., Hesse, M., Argall, M. R., Shuster, J., Ergun, R. E., Alm, L., Nakamura, R., Genestreti, K. J., Gershman, D. J., Paterson, W. R., Turner, D. L., Cohen, I., Giles, B. L., Pollock, C. J., Wang, S., Chen, L. J., Stawarz, J. E., Eastwood, J. P., Hwang, K. J., Farrugia, C., Dors, I., Vaith, H., Mouikis, C., Ardakani, A., Mauk, B. H., Fuselier, S. A., Russell, C. T., Strangeway, R. J., Moore, T. E., Drake, J. F., Shay, M. A., Khotyaintsev, Y. V., Lindqvist, P. A., Baumjohann, W., Wilder, F. D., Ahmadi, N., Dorelli, J., Avanov, L. A., Oka, M., Baker, D. N., Fennell, J. F., Blake, J. B., Jaynes, A. N., Le Contel, O., Petrinec, S. M., Lavraud, B., and Saito, Y., *Science* **362**, 1391 (2018).
- Turner, D. L., Cohen, I. J., Bingham, S. T., Stephens, G. K., Sitnov, M. I., Mauk, B. H., Denton, R. E., Leonard, T. W., Fennell, J. F., Blake, J. B., Torbert, R. B., and Burch, J. L., *Geophys. Res. Lett.* **48**, e2020GL090089, <https://doi.org/10.1029/2020GL090089> (2021).
- Turner, D. L., Fennell, J. F., Blake, J. B., Clemmons, J. H., Mauk, B. H., Cohen, I. J., Jaynes, A. N., Craft, J. V., Wilder, F. D., Baker, D. N., Reeves, G. D., Gershman, D. J., Avanov, L. A., Dorelli, J. C., Giles, B. L., Pollock, C. J., Schmid, D., Nakamura, R., Strangeway, R. J., Russell, C. T., Artemyev, A. V., Runov, A., Angelopoulos, V., Spence, H. E., Torbert, R. B., and Burch, J. L., *Geophys. Res. Lett.* **43**, 7785, <https://doi.org/10.1002/2016GL069691> (2016).
- Veronig, A. M. and Brown, J. C., *Astrophys. J.* **603**, L117 (2004).
- Wang, R., Lu, Q., Li, X., Huang, C., and Wang, S., *J. Geophys. Res.: Space Phys.* **115**, A11201, <https://doi.org/10.1029/2009JA014553> (2010).
- Wang, R., Lu, Q., Nakamura, R., Huang, C., Du, A., Guo, F., Teh, W., Wu, M., Lu, S., and Wang, S., *Nat. Phys.* **12**, 263 (2016).
- Yoon, P. H., Rhee, T., and Ryu, C.-M., *J. Geophys. Res.* **111**, A09106, <https://doi.org/10.1029/2006JA011681> (2006).
- Young, D. T., Burch, J. L., Gomez, R. G., De Los Santos, A., Miller, G. P., Wilson, P., Paschalidis, N., Fuselier, S. A., Pickens, K., Hertzberg, E., Pollock, C. J., Scherrer, J., Wood, P. B., Donald, E. T., Aaron, D., Furman, J., George, D., Gurnee, R. S., Hourani, R. S., Jacques, A., Johnson, T., Orr, T., Pan, K. S., Persyn, S., Pope, S., Roberts, J., Stokes, M. R., Trattner, K. J., and Webster, J. M., *Space Sci. Rev.* **199**, 407 (2016).
- Zhou, M., Li, T., Deng, X., Pang, Y., Xu, X., Tang, R., Huang, S., and Li, H., *J. Geophys. Res.: Space Phys.* **121**, 3108, <https://doi.org/10.1002/2015JA022085> (2016).
- Zweibel, E. G. and Yamada, M., *Annu. Rev. Astron. Astrophys.* **47**, 291 (2009).